Electronic structure and mechanical properties of ternary ZrTaN alloys studied by *ab initio* calculations and thin-film growth experiments

G. Abadias,[1,*] M. B. Kanoun,[2,†] S. Goumri-Said,[3] L. Koutsokeras,[1,4,‡] S. N. Dub,[5] and Ph. Djemia[6]

[1]*Département Physique et Mécanique des Matériaux, Institut P', CNRS-Université de Poitiers-ENSMA, SP2MI - Téléport 2, BP 30179, F86962 Futuroscope-Chasseneuil, France*

[2]*School of Physics, Georgia Institute of Technology, Atlanta, Georgia 30332–0400, USA*

[3]*School of Chemistry and Biochemistry and Center for Organic Photonics and Electronics, Georgia Institute of Technology, Atlanta, Georgia 30332–0400, USA*

[4]*Department of Materials Science and Engineering, University of Ioannina, Ioannina 45110, Greece*

[5]*Institute for Superhard Materials, NAS of Ukraine, Avtozavodskaya St. 2, 04074 Kiev, Ukraine*

[6]*Laboratoire des Sciences des Procédés et des Matériaux (LSPM) - UPR 3407 CNRS, Université Paris 13, Sorbonne Paris Cité, 99 Avenue J.B.Clément 93430 Villetaneuse, France*

(Received 29 August 2013; revised manuscript received 26 September 2014; published 21 October 2014)

The structure, phase stability, and mechanical properties of ternary alloys of the Zr-Ta-N system are investigated by combining thin-film growth and *ab initio* calculations. $Zr_{1-x}Ta_xN$ films with $0 \leqslant x \leqslant 1$ were deposited by reactive magnetron cosputtering in $Ar + N_2$ plasma discharge and their structural properties characterized by x-ray diffraction. We considered both ordered and disordered alloys, using supercells and special quasirandom structure approaches, to account for different possible metal atom distributions on the cation sublattice. Density functional theory within the generalized gradient approximation was employed to calculate the electronic structure as well as predict the evolution of the lattice parameter and key mechanical properties, including single-crystal elastic constants and polycrystalline elastic moduli, of ternary $Zr_{1-x}Ta_xN$ compounds with cubic rocksalt structure. These calculated values are compared with experimental data from thin-film measurements using Brillouin light scattering and nanoindentation tests. We also study the validity of Vegard's empirical rule and the effect of growth-dependent stresses on the lattice parameter. The thermal stability of these $Zr_{1-x}Ta_xN$ films is also studied, based on their structural and mechanical response upon vacuum annealing at 850 °C for 3 h. Our findings demonstrate that $Zr_{1-x}Ta_xN$ alloys with Ta fraction $0.51 \leqslant x \leqslant 0.78$ exhibit enhanced toughness, while retaining high hardness ~30 GPa, as a result of increased valence electron concentration and phase stability tuning. Calculations performed for disordered or ordered structures both lead to the same conclusion regarding the mechanical behavior of these nitride alloys, in agreement with recent literature findings [H. Kindlund, D. G. Sangiovanni, L. Martinez-de-Olcoz, J. Lu, J. Jensen, J. Birch, I. Petrov, J. E. Greene, V. Chirita, and L. Hultman, APL Materials **1**, 042104 (2013)].

DOI: 10.1103/PhysRevB.90.144107 PACS number(s): 62.20.−x, 81.05.Je, 68.60.Bs, 71.15.Mb

I. INTRODUCTION

Transition metal nitrides (TMN) have been extensively studied in the last decades, owing to their excellent performance as hard, wear-resistant protective coatings in the cutting tool industry [1,2], but also as suitable template layers for the growth of group-III-nitride wide bandgap semiconductors for optoelectronic applications [3–5]. Since the materials selection concept of Holleck [6] to design multicomponent hard coatings, efforts have been made to synthesize new ternary or multinary TMN-based alloys [7–15], which offer the possibility of fine tuning the mechanical and physical properties by an appropriate choice of metal or nonmetal alloying elements and by optimizing deposition process parameters. Physical vapor deposition (PVD) techniques, such as magnetron sputtering, offer the flexibility to control stoichiometry, microstructure, and texture [13–18] and are industrially scalable.

Nitride compounds in which the transition metal belongs to the groups IVb-Vb-VIb, i.e., having partially filled *d* bands, are an interesting class of TMN materials combining metallic, covalent, and ionic bonding, which can form metastable ternary solid solutions with cubic rocksalt structure, as reported recently for a wide range of Ti-*M*-N and Ta-*M*-N (M = Ti, Zr, Hf, Nb, Ta, Mo, W) systems [5,14–18]. This solubility propensity is related to the preferential hybridization of the *d* and *sp* electrons of the metals and nitrogen, respectively, despite the different possible metal's *d* valence electron configurations involved [15,16]. Among these ternary compounds, the TiTaN system appears as an alternative candidate to superhard nanocomposite materials [2,8,19], as a hardness of 42 GPa was reported for sputtered TiTaN thin films with a Ta/(Ti + Ta) ratio of 0.69 [17]. However, in the design of novel coatings, not only a high hardness but also ductility are a requisite, i.e. *toughness* is sought. Transition metal nitrides, being intrinsically hard ceramics, usually suffer from brittleness under mechanical loading, reducing their potential use as wear-resistance coatings.

Recent *ab initio* calculations by Sangiovanni *et al.* [11,12] have shown that Mo and W alloying into TiN decisively induced a ductile behavior, while retaining stiffness and hardness. This is reflected by a decrease of the shear modulus

*gregory.abadias@univ-poitiers.fr

†mohammed-benali.kanoun@physics.gatech.edu

‡Present address: Department of Mechanical Engineering and Materials Science and Engineering, Cyprus University of Technology.

G (and related elastic constant C_{44}) and an increase of the bulk modulus B for $Ti_{0.5}Mo_{0.5}N$ and $Ti_{0.5}W_{0.5}N$ compounds, resulting in a G/B ratio lower than 0.5, i.e., corresponding to a ductility trend according to Pugh's criterion for metals [20]. Toughness improvement was confirmed experimentally by Kindlund *et al.* [21] for magnetron sputtered $V_{0.5}Mo_{0.5}N$ epitaxial alloys.

The origin of this supertoughening stems from a change in charge distribution upon substitution of Ti with Mo or W atoms, which increases the metal-metal *d*-*d* interaction during the shearing deformation. The reason is that these ternaries have one more valence electron per unit cell, by comparison to TiN, yielding to a higher filling of the d-t_{2g} metallic states. This tendency is confirmed by recent elastic calculations performed by Holec *et al.* [22] on a series of binary TMN compounds and Petrman and Houska [23] on ternary and quaternary ones: the Cauchy pressure $C_{12}-C_{44}$ increases to positive values when the valence electron concentration (VEC) per unit formula increases, and positive Cauchy pressures correspond to predominant metallic bonding and ductile behavior, according to Pettifor's criterion [24]. Notably, for ternaries and quaternaries TMN, the best results were obtained for VEC of 10 and 10.5 [12,23,25,26]. These values are larger than what was reported earlier by Holleck [6] for mixed carbides and carbonitrides that exhibited a maximum hardness at a VEC of ~8.5. Finally, let us mention that Joelsson *et al.* [9] identified from a number of 4*d* TMN compounds potential ternary candidates with enhanced hardness when the VEC reaches ~9.5–9.8, corresponding to the existence of a polytypic region (i.e., cubic and hexagonal phases may coexist due to their similar total energy).

These recent theoretical findings imply the possibility of controlling the ductility trends in TMN by tuning the electronic structure in terms of VEC and motivating research activities in the quest for designing new hard and ductile coatings. On a more fundamental level, this drives the prospects for a better understanding of the electronic origins of brittleness vs ductility. This represents, however, a challenging task for the materials science community. Among possible TMN candidates, the Zr-Ta-N system remains relatively unexplored comparably to Ti-Zr-N or Ti-Ta-N, despite promising functional properties [27]. To the best of our knowledge, the equilibrium Zr-Ta-N bulk phase diagram has not been assessed in the literature. The parent binary compounds crystallize in different structures: the cubic B1 one (space group $Fm\bar{3}m$, Na-Cl prototype) for ZrN, and the hexagonal one (space group $P6/mmm$) for TaN, although its metastable cubic B1 allotrope (referred hereafter as δ-TaN) can be synthesized in thin-film form [28,29]. Conductive ternary $Zr_{1-x}Ta_xN$ films with a cubic rocksalt structure are structurally and electrically appropriate as growth templates or Ohmic contacts for *n*-type $In_yGa_{1-y}N$ semiconductors due to the possibility of tailoring their lattice constant in a large range (0.433 to 0.457 nm) and matching their work function with the electron affinity of the semiconductor. Interestingly, ZrN and TaN, with, respectively, 9 and 10 VEC, are expected to meet the optimum VEC when combined to form $Zr_{1-x}Ta_xN$ compounds. Thus, the knowledge of electronic structure and elastic properties of the Zr-Ta-N system are of prime importance to predict phase stability, as well as material toughness and hardness.

Very limited information is available on the phase formation and electronic structure of TaZrN alloys [10,27,30]. *Ab initio* calculations based on the density functional theory (DFT) were carried out by Aouadi [10], but only partial information on the elastic properties were reported, namely the Young's modulus E and shear modulus G, and compared to nanoindentation data. The aim of the present paper is to provide a comprehensive picture of the mechanical properties and electronic structure of ternary $Zr_{1-x}Ta_xN$ compounds by combining *ab initio* DFT calculations and thin-film growth experiments. For this purpose, a full determination of the elastic properties, including single-crystal elastic constants c_{ij}, elastic moduli (B, G, E) and Poisson ratio ν of isotropic polycrystalline materials, is established when alloying Ta atoms into ZrN lattice. These computed values are compared with an experimental determination of the C_{44} elastic constant and Young's modulus of magnetron sputtered ternary $Zr_{1-x}Ta_xN$ polycrystalline films derived from Brillouin light scattering (BLS) and nanoindentation tests, respectively. The brittle/ductile behavior of these ternaries is analyzed based on Pugh [20] and Pettifor [24] criteria. We also discuss the validity of Vegard's empirical rule, based on the experimental and calculated lattice constants, in relation with the type of bonding between metals and N atoms. We also address the issue of intrinsic growth stress as a possible source of extrinsic hardness enhancement in these sputtered materials. To this end, a direct and real-time measurement of the film stress was first carried out during thin-film growth. The residual stress was also determined from x-ray diffraction (XRD) strain analysis, using the calculated c_{ij} elastic constants as necessary inputs to relate strain and stress.

II. EXPERIMENTAL DETAILS

A series of $Zr_{1-x}Ta_xN$ films were deposited at $T_s = 300\,^{\circ}C$ on (001) Si substrates covered with native SiO_x (~2 nm) using dc magnetron cosputtering from separate Zr (99.2% purity) and Ta (99.998% purity) cathode targets under a reactive $Ar + N_2$ atmosphere. The cathodes were 75 mm diameter, water-cooled planar magnetron sources, electrically connected to a dc power supply and placed in a confocal configuration at a distance $d = 18$ cm from the substrate. Prior to deposition, the vacuum chamber was pumped using a cryogenic pump down to $\sim 5 \times 10^{-6}$ Pa. Then, targets were sputter-etched for 5 min under Ar plasma discharge with a shutter shielding the substrate to remove any possible oxides or contaminants from the target surface.

The magnetrons were operating in balanced mode and a negative bias of −60 V was applied to the substrate during deposition. Sputtering was carried out in $Ar + N_2$ discharges with a pumping speed fixed at ~100 l/s. The Ta fraction in the ternary $Zr_{1-x}Ta_xN$ films was monitored by adjusting the respective power of the Zr and Ta targets (see Table I). The total working pressure was fixed at 0.30 Pa by setting the Ar flow to 16 sccm, while the N_2 flow was adjusted to obtain stoichiometric nitride compounds. For $x < 1$, the fraction of N_2 flow f_{N_2} was ~4–6%, corresponding to sputtering conditions in metallic target mode, just before the onset of the hysteresis, as checked from the evolutions of the N_2 partial pressure and target voltage with N_2 flow (not reported here). For $x = 1$, due

TABLE I. Process parameters used during dc reactive magnetron cosputtering of $Zr_{1-x}Ta_xN$ films. The Ta content x and the N concentration measured from EPMA, the mass density ρ derived from XRR data, and the calculated growth rate R are also reported. The in-plane biaxial stress σ derived from XRD elastic strain analysis is also reported using c_{ij} data of cubic ordered compounds taken from Table III.

TaN	Zr target		Ta target		Ar Flow	N_2 fraction,	P_{tot}	Ta/	N concentration	Growth rate,	Mass density,	Film thickness	XRD stress,
fraction, x	Power (W)	Voltage (V)	Power (W)	Voltage (V)	(sccm)	f_{N_2}	(Pa)	(Ta + Zr)	(at.%)	R (Å/s)	ρ (g/cm^3)	(nm)	σ (GPa)
0	300	385	/	/	16.0	0.04	0.30	0	50.5	3.03	7.1	455	/
0.14	300	385	40	340	16.0	0.05	0.30	0.14	/	/	/	310	/
0.24	300	385	80	369	16.0	0.06	0.30	0.24	51.7	3.25	9.1	315	-4.7 ± 0.3[a]
													-2.3 ± 0.4[b]
0.51	200	375	158	405	16.0	0.06	0.30	0.51	49.1	3.05	11.3	275	-6.1 ± 1.0[a]
													-4.2 ± 0.9[b]
0.78	107	340	250	425	16.0	0.04	0.30	0.78	54.5	2.85	13.7	310	-8.3 ± 2.8[a]
													-4.8 ± 1.7[b]
1	/	/	200	427	16.0	0.20	0.38	1	53.8	0.97	14.3	290	/

[a]As-grown state.
[b]Vacuum annealed at 850 °C for 3 h.

to the lower affinity of Ta with nitrogen with respect to Zr, f_{N_2} was increased up to 20% to ensure a N/Ta stoichiometric ratio in the TaN film. In this case, the total working pressure was ~0.38 Pa. The chosen value of f_{N_2} is close to that used by Shin *et al.* [28] to obtain magnetron sputtered δ-TaN films with cubic structure.

A rotation speed of 10 rpm of the substrate holder was used during deposition, ensuring a relative compositional and thickness homogeneity better than 2% over 3×3 cm^2 sample areas. The film thickness h_f was varied between ~20 and ~450 nm by controlling the deposition time at constant power deposition conditions. The thicker films with $h_f > 250$ nm (see Table I) were systematically used for BLS and nanoindentation experiments.

Postdeposition thermal annealing at 850 °C for 3 h was performed in a quartz tube furnace, pumped down to 3×10^{-4} Pa using a turbomolecular pump.

The growth morphology was investigated by cross-sectional and plan view scanning electron microscopy (SEM) using the JEOL 7001F-TTLS microscope operated at 20 kV and secondary electron image mode. The growth rate R was calculated from the deposition time and film thickness measurement obtained from SEM on thicker samples or x-ray reflectivity (XRR) on thinner ones ($h_f \sim 50$–100 nm). An optical model based on Parratt's formalism and considering a three-layer stacking (topmost oxidized layer, TaZrN layer, interfacial SiO_x layer) on Si substrate was adjusted to reproduce the XRR scans. The fitting procedure enables one to accurately extract the film thickness h_f, the mass density ρ, as well as surface and interface roughness. Values of ρ and R are reported in Table I.

The elemental composition of the as-deposited TaZrN films was determined from electron probe microanalysis (EPMA) using a wavelength-dispersive Oxford Instrument spectrometer unit attached to the SEM. The results are listed in Table I. The N concentration was found to be approximately 50 at.% for all films, as also confirmed by Rutherford backscattering spectroscopy, so we will refer in the following to $Zr_{1-x}Ta_xN$ to denote the samples despite possible deviation from stoichiometry from one sample to another.

The crystal structure and preferred orientation of as-deposited and annealed films were determined from XRD recorded on a D8 Discover Bruker diffractometer operating in the Bragg-Brentano configuration, Cu Kα wavelength (0.15418 nm) and equipped with a divergence slit of 1.0°, a scattered-radiation slit of 0.6 mm, an energy dispersive Si(Li) detector cooled down thermoelectrically by Peltier elements (Sol-X detector), and defined with a 0.2 mm opening angle slit. In order to avoid reflections from the Si substrate, the XRD scans were recorded in the ω-2θ geometry using a 0.5° offset along ω. Since the typical grain mosaic spread was around 15°, independently of sputtering conditions, this offset along ω had only minor influence on the maximum diffracted intensity.

The complete strain-stress state of the as-deposited and annealed $Zr_{1-x}Ta_xN$ films was determined from XRD using a pseudo-sin$^2\psi$ method adapted for the case of fiber-textured layers. This method, also known as the ideal direction method [31], consists of measuring the variations of the lattice parameter a_ψ of a given set of crystallites—those having their fiber axis along the growth direction—as a function of

$\sin^2\psi$. The values of a_ψ are determined from different and specic (*hkl*) crystallographic planes whose normal direction [*hkl*] makes an angle ψ with the fiber-axis direction; in other words, the selected (*hkl*) reflections correspond to the intensity poles of the stereographic projection taken along the fiber axis. This procedure differs from the classical $\sin^2\psi$ method used for bulk powders or randomly oriented polycrystalline thin films, where a single (*hkl*) reflection is measured at various ψ angles [32]. X-ray diffraction measurements were carried out on a 4-circle Seifert XRD 3000 diffractometer operating in point-focus geometry with a Cu x-ray source, a 1.0-mm-diameter collimator, and a scintillation counter detector. Then using linear elastic theory and the set of elastic constants c_{ij} determined from *ab initio* calculations (see Sec. III), the in-plane stresses along two principal directions σ_1 and σ_2, as well as the stress-free lattice parameter a_0, can be determined [32,33].

A direct determination of the biaxial film stress can be obtained from wafer curvature measurements. A highly sensitive multiple-beam optical stress sensor (MOSS) designed by kSA was implemented in the deposition chamber, allowing us to probe in real time the stress evolution during growth. More details on the experimental setup can be found in Ref. [34]. Let us just recall here that the film force per unit width F/w is the quantity that is determined experimentally; it corresponds to the product $\sigma_{\text{avg}} \times h_f$, where σ_{avg} is the average film stress. Using a 200 μm thick Si wafer, the curvature resolution was 2×10^{-4} m^{-1}, which translates into a sensitivity of ~30 MPa for a 10-nm-thick deposited film.

Brillouin light scattering has proved to be a very efficient technique for achieving a complete elastic characterization of thin films and multilayered structures [35]. In a BLS experiment, a monochromatic light beam is used to probe the thermally excited acoustic waves, which are naturally present in the investigated medium. The power spectrum of these excitations is mapped out from frequency analysis of the light scattered within a large enough solid angle. Because of the wave vector conservation rule in the phonon-photon interaction, the wavelength of the revealed elastic waves is of the same order of magnitude as that of light and then is much larger than the interatomic distances, so that the material can be described as a continuous effective-medium. Here, we used the backscattering interaction geometry where $\boldsymbol{k_i}$ ($\approx -\boldsymbol{k_s}$) denotes the incident (scattered) optical wave vector in air, so that the modulus value of the wave vector [$\boldsymbol{Q} = \pm(\boldsymbol{k_s} - \boldsymbol{k_i})_{||}$] of the probed surface acoustic waves travelling parallel to the film plane is fixed experimentally to the value $Q = 2k_i \sin(\theta)$, where θ is the incidence angle of the light with respect to surface normal. The acoustical wavelength (Λ) is simply defined as $\Lambda = 2\pi/Q$, and the velocity (V) of a surface acoustic wave is obtained from the frequency measurements f thanks to the relation $V = f \times \Lambda$. The BLS spectra were obtained at room temperature in air, with typical acquisition times of 2 h. The light source was an yttrium aluminium garnet (YAG) solid laser with a single mode of 532 nm. Typically, 300 mW of a naturally p-polarized light was focused on the surface of the sample, and the backscattered light was analyzed by means of a Sandercock-type 3 + 3 pass tandem Fabry-Perot interferometer.

For nearly opaque layers, such as the present ZrTaN films with a metallic character, the scattering mechanism is restricted to the scattering of light by the dynamical corrugation of the free surface by acoustic waves travelling parallel to the film plane [36]. Thus, we can only observe the surface acoustic waves with a sagittal polarization (the first component u_x of the displacement field $\boldsymbol{u}$ is along the wave vector $\boldsymbol{Q}$ direction, the second component $u_y = 0$, and the third component u_z is vertical). For films with thicknesses around the acoustic wavelength (~300 nm) and deposited on a substrate with higher acoustic phase velocity ("slow" film on "fast" substrate), the surface acoustic waves with a sagittal polarization are the Rayleigh wave (R) and the so-called Sezawa guided waves ($S_1 - S_n$) [36] at higher frequencies. The frequency (velocity) and number of these S_i surface modes are dependent on both the thickness and the elastic constants of the film and of the substrate, whereas the velocity of the Rayleigh surface wave V_R is mainly dependent on the transverse velocity $V_T = (C_{44}/\rho)^{1/2}$ [37] through the relation $V_R = \beta V_T$, where β is a slightly varying function of the whole elastic constants of the film but remains close to ≈0.94.

The film thickness h_f and the mass density ρ of the films were preliminarly measured by XRR with accuracy better than 2%, as necessary inputs to determine the fitted eigenvalues (frequencies f) by solving numerically the acoustical problem for a multilayer consisting of a film on a substrate with a perfect interface [38,39]. The other parameters are the elastic tensors of the film (noted as C_{ij}-to be determined) and the substrate (considered as a known input). The fitting procedure of the frequencies f was started with the calculated effective elastic constants $\langle C_{ij} \rangle$ of the film as initial elastic parameters input. The $\langle C_{ij} \rangle$ values were evaluated from the single-crystal elastic constants c_{ij} computed from DFT calculations and assuming either random or preferred orientation of the crystallites (see Sec. III.B).

Although C_{11}, C_{13}, and C_{33} could in principle be extracted from the fit of BLS spectra and frequencies f of Rayleigh and Sezawa surface modes [36,38–40], their determination is not as direct as C_{44} and remains associated with a larger uncertainty. Also, $C_{66} = (C_{11} - C_{12})/2$ can be only determined from measurements of the phase velocity of shear horizontal modes (Love modes) [38,39] but are not observed here because of their low bulklike scattering mechanism efficiency. Therefore, we can only reasonably compare the experimental effective C_{44} value obtained from BLS with the calculated effective elastic constant $\langle C_{44} \rangle$. Its experimental accuracy is estimated to be much better than 8% and depends mainly on the considered inaccuracy of the other elastic constants.

III. COMPUTATIONAL METHODS

A. DFT calculations

$Zr_{1-x}Ta_xN$ alloys were considered as quasibinary alloys, as mixing of metallic (Zr or Ta) elements took place only with the cation sublattice, the other sublattice being fully occupied by N atoms. Two different types of metal sublattice configurations in a supercell approach were probed for the cubic B1 structure to capture a different degree of structural

short-range order (SRO): *ordered* and *special quasirandom structures* (SQSs) [41]. The ordered supercell employed in our calculations for ternary compounds ($x = 0.25$, 0.50, and 0.75) contained 64 atoms, based on a $2 \times 2 \times 2$ supercell with a minimum number of intermetallic bonds (clustered configuration C#3) [42]. This structure closely matches the Cu-Pt-type atomic ordering observed experimentally in TiWN [43] and VWN [44] thin films and was found to be the most energetically stable configuration for many TMN ternaries [11,12,42]. For SQS, a $2 \times 3 \times 2$ (48 atoms) supercell was considered for $Zr_{1-x}Ta_xN$ alloys having the following compositions $x = 0.25, 0.5$, and 0.75. The SQS approach with small or vanishing SROs to account for randomness in the metallic sublattice was successfully implemented for predicting thermodynamics of TiAlN and other related systems [45,46].

Total energy and elastic constants calculations were carried out by means of the DFT based on the generalized gradient approximation (GGA) of Perdew-Burke-Ernzerhof (PBE) [47], as implemented in the Vienna *Ab initio* Simulation Package (VASP) [48]. The electron and core interactions are included using the projector-augmented wave (PAW) formalism [49]. An energy cutoff of 500 eV for the plane-wave expansion of the PAWs was used. The integrals over Brillouin zone (BZ) were approximated by sums over a $13 \times 13 \times 13$ k-point mesh according to Monkhorst-Pack [50] for the ordered configuration (C#3). Both atomic coordinates and cell parameters were optimized until all the components of the residual forces on the atoms were less than 0.01 eV/Å.

Regarding the description of elasticity, recent calculations by Tasnádi *et al.* [46] have shown the influence of shape and size of SQS supercells to reliably model elastic constants. As the SQS method generally breaks the point group symmetry, the elastic tensor contains 21 independent elastic constants. Details on elastic constant determination are provided in the Supplemental Material [51]. Although a relatively small supercell was used in this paper, errors in predicting the closest cubic elastic tensor of B1 structure are expected to be within 10% [46].

For $Zr_{1-x}Ta_xN$ alloys with hexagonal structure, our calculations were limited to their energy of formation, so as to predict the compositional range where they can be energetically more favorable with respect to cubic alloys. To describe the hexagonal structure with space group $P6/mmm$, a $2 \times 2 \times 2$ supercell with 48 atoms was employed. Only ordered configurations were considered for $Zr_{1-x}Ta_xN$ alloy compositions with $x = 0$, 0.25, 0.5, 0.75, and 1. For these concentrations, the six Zr and/or Ta atoms are at the metal sublattice positions (0.5, 0.0, 0.7456), (0.1652, 0.3305, 0.0), (0.3333, 0.6667, 0.0), (0.0, 0.0, 0.7444), (0.1669, 0.3339, 0.5), (0.3333, 0.6667, 0.5) of the 48 atom supercell. These atomic positions constitute the primitive cell of the hexagonal binary/ternary structure. The multiplicity of the site is due to the space group symmetry, and it reproduces all other atomic position sites that constitute the supercell of 24 metal and 24 nitride atoms.

The optimized cubic structures obtained from the VASP code were used in the WIEN2k package [52] for the analysis of the electronic structure using the full-potential linearized augmented plane wave method with the mixed basis local orbital (FP-(L)APW + lo). The exchange and correlations were treated within the GGA-PBE approach [47]. A k-mesh sampling with 1500 and 80 special k-points in the full Brillouin zone was considered for binary (ZrN and TaN) and ternary $Zr_{1-x}Ta_xN$ compounds with cubic symmetry, respectively, to obtain the density of states (DOS) and charge density distribution. The muffin-tin radii (R_{MT}) 2.08 (Zr), 2.20 (Ta), and 1.95 (N) Bohr units were used, and we assume a plane wave cutoff of $K_{max} = 8.0/R_{MT}$. The convergence of self-consistent calculations was attained with a total energy convergence tolerance of 0.1 mRy.

B. Calculation of polycrystalline elastic properties from single-crystal elastic constants

The determination of the elastic properties of polycrystalline aggregates from the knowledge of the anisotropic single-crystal elastic constant c_{ij} can be assessed from several micromechanical models, based on different grain interaction assumptions. Here we have used the Hill average [53] for the calculation of isotropic polycrystalline elastic moduli. The expressions of the bulk modulus B_H, shear elastic modulus G_H, and Young's modulus E are given in Ref. [51] for the case of cubic, as well as noncubic (SQS) $Zr_{1-x}Ta_xN$ structures, the consideration of the hexagonal phase (observed experimentally for TaN-rich films only) being out of the scope of this paper.

The calculation of the *effective* elastic constants $\langle C_{ij} \rangle$ of polycrystalline cubic $Zr_{1-x}Ta_xN$ alloys was carried out using the Hill average (using c_{ij} values from ordered supercells) but assuming two distinct symmetries corresponding to *isotropic* and *transversely isotropic* elastic properties. These assumptions are based on experimental findings (the crystal structure and the crystallographic texture of $Zr_{1-x}Ta_xN$ films): the case of isotropic symmetry corresponds to randomly oriented films (observed for ZrN-rich films), while the case of transversely isotropic symmetry corresponds to fiber-textured films. In the former case, two independent effective elastic constants $\langle C_{11} \rangle$ and $\langle C_{44} \rangle = (\langle C_{11} \rangle - \langle C_{12} \rangle)/2$ are necessary to model the surface acoustic waves and calculate their frequencies f, while the latter case requires the knowledge of five independent effective elastic constants, namely $\langle C_{11} \rangle$, $\langle C_{33} \rangle$, $\langle C_{44} \rangle$, $\langle C_{13} \rangle$, and $\langle C_{12} \rangle$ [$\langle C_{66} \rangle = (\langle C_{11} \rangle - \langle C_{12} \rangle)/2$], which is equivalent to hexagonal symmetry. Both (111) and (200) fiber textures were considered for the calculations [54].

IV. RESULTS AND DISCUSSION

A. Phase stability and equilibrium properties from DFT calculations

The stability of $Zr_{1-x}Ta_xN$ alloys can be determined from the formation energy E_f, expressed as

$$E_f = E(Zr_{1-x}Ta_xN) - (1-x)E(Zr) - xE(Ta) - \tfrac{1}{2}E(N_2), \quad (1)$$

where $E(Zr_{1-x}Ta_xN)$ represents the total energy per atom of $Zr_{1-x}Ta_xN$ compounds with either cubic or hexagonal structure, $E(Zr)$ and $E(Ta)$ the total energy of Zr and Ta in their stable crystalline form, and $E(N_2)$ that of the nitrogen molecule. Figure 1 shows the evolution of E_f vs Ta fraction for cubic (ordered and SQS supercells) and hexagonal structures,

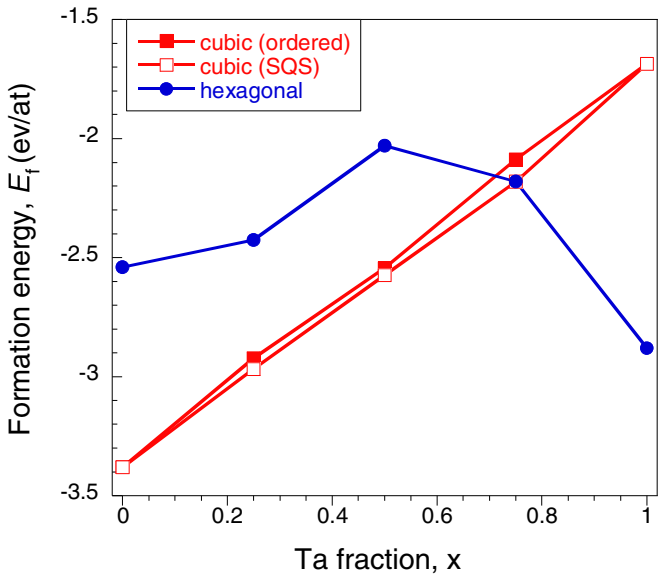

FIG. 1. (Color online) Formation energy (E_f) of cubic ordered, SQS disordered, and hexagonal structures of $Zr_{1-x}Ta_xN$ alloys.

the corresponding values of E_f being reported in Table II for the cubic phase only. For the cubic phase, the values of E_f increase almost linearly from −3.381 eV/at (ZrN) to −1.686 eV/at (TaN). It can be seen that the E_f values based on ordered supercells are slightly overestimated as compared to those using the SQS methodology. The mixing enthalpy $\Delta H_{\text{mix}} = E_f(Zr_{1-x}Ta_xN) - (1 - x)\ E_f(ZrN) - xE_f(TaN)$ is found to be positive over the whole composition range, but relatively low (9–35 meV/at), in good agreement with recent calculations of Petrman and Houska [23]. This suggests that cubic $Zr_{1-x}Ta_xN$ solid solutions are metastable and will have a tendency to decompose into ZrN and δ-TaN phases.

From Fig. 1, one can see that the formation energy of the hexagonal structure overlaps with that of the cubic structure in a concentration range $x \sim 0.65$–0.75, while above $x = 0.75$, the hexagonal structure is the most energetically favorable. A transition from cubic to hexagonal structure is therefore predicted from DFT calculations upon Ta alloying in the ZrN lattice.

The calculated $E(V)$ curves of the total energy vs volume of cubic alloys were fitted using third-order Birch-Murnaghan equation of state [55] to determine the structural parameters

TABLE II. Calculated (calc) structural parameters of $Zr_{1-x}Ta_xN$ alloys with cubic rocksalt structure for ordered (bold values) and SQS disordered (marked with *) configurations. B' is the pressure derivative of the bulk modulus B (obtained from Birch-Murnaghan equation of state). The formation energy E_f is also shown. Also reported are experimental (exp) and theoretical data from the literature for binary nitrides.

	a_{calc} (nm)	ρ (g/cm^3)	B (GPa)	B'	E_f (eV)
ZrN	**0.4607**	**7.10**	**253**	**4.072**	**−3.381**
	0.4578[a]		250[c]		
	0.4584[b]		250[g]		
	0.4618[c]		248[i]		
	0.4583[g]				
	0.4596[i]				
$Zr_{0.75}Ta_{0.25}N$	**0.4554**	**8.91**	**270**	**4.531**	**−2.922**
	0.4565*	8.92*	269*	4.387*	−2.968*
$Zr_{0.50}Ta_{0.50}N$	**0.4514**	**10.82**	**289**	**4.623**	**−2.544**
	0.4521*	10.82*	279*	4.523*	−2.574*
$Zr_{0.25}Ta_{0.75}N$	**0.4473**	**12.84**	**310**	**4.717**	**−2.088**
	0.4480*	12.82*	307*	4.431*	−2.180*
δ-TaN	**0.4443**	**14.97**	**334.6**	**4.112**	**−1.686**
	0.4426[c]		325[c]		
	0.4350[d]		379.6[e]		
	0.4326[e]		329[g]		
	0.4330[f]		375[h]		
	0.4408[g]		328[i]		
	0.4395[h]				
	0.4413[i]				
	0.4336[j]				

[a]Reference [56]; exp (bulk).
[b]Reference [56]; exp (a_0).
[c]Reference [22]; calc GGA.
[d]Reference [28]; exp (a_0).
[e]Reference [59]; calc LDA.
[f]Reference [29]; exp (a_0).
[g]Reference [60]; calc GGA.
[h]Reference [61]; calc GGA.
[i]Reference [23]; calc GGA.
[j]Reference [58]; exp (bulk).

for ZrN, δ-TaN, and $Zr_{1-x}Ta_xN$ alloys using ordered and SQS supercells. Table II collects the optimized lattice parameter (a_{calc}), bulk modulus B, pressure derivative B', and mass density ρ of $Zr_{1-x}Ta_xN$ ($0 \leqslant x \leqslant 1$). A gradual decrease of a_{calc} is predicted as the concentration of Ta increases in the ZrN lattice, as expected from the difference in ionic radius between the two metal elements. Concomitantly, a gradual increase in ρ is obtained. The compositional dependence of the lattice parameter obtained for ordered and SQS supercells of cubic $Zr_{1-x}Ta_xN$ alloys is shown in Fig. 2 and compared with previous data computed by Aouadi [10] using DFT pseudopotential calculations together with experimental data (a_0) from this paper as well as from the literature [23,28,29,56–58]. It can be observed that both ordered and SQS disordered values are above those reported by Aouadi [10]; however, the maximum relative deviation, obtained for $x = 1$ (δ-TaN), is only 1%. Our a_{calc} values also slightly overestimate the stress-free lattice parameters a_0 derived experimentally from XRD for alloy thin films with $x = 0.24$, 0.51, and 0.78 (see Sec. IV.D). The linear interpolation of these a_0 values to $x = 0$ and $x = 1$ closely matches the stress-free lattice parameters of ZrN [56] and δ-TaN [28,29] thin films deposited by PVD techniques. If one refers to the lattice parameter of bulk binary nitrides (see Table II), the difference amounts to 0.6% for ZrN and 2.5% for δ-TaN. Such overestimates are consistent with usual trends obtained when using GGA exchange correlation functional comparatively to local density approximation (LDA) [22,59–63].

As seen from Fig. 2, the variation of a_{calc} vs x for the SQS supercell configuration follows approximately the Vegard's linear interpolation between lattice parameters of cubic binary nitrides, while a slight negative deviation is observed for ordered supercells. Opposite trends, i.e. positive deviation from Vegard's empirical rule, were reported for Ti-Zr-N [14] and Ti-Ta-N [64] ternary systems combining two transition metals, as well as in quaternary systems when alloying early transition metal elements (Y, Zr, Nb, Hf, and Ta) in Ti-Al-N [45]. For TaZrN, the presence of a negative deviation from Vegard's estimate is consistent with the empirical prediction proposed by Fournet [65] from simple elastic considerations: using the data reported in Table II, the dimensionless parameter $\alpha = \frac{a_{ZrN} \times B_{ZrN}}{a_{TaN} \times B_{TaN}}$ is found to be in the range $0.70 - 0.78$, i.e. $\alpha < 1$, corresponding to negative deviation from linear Vegard's behavior.

Finally, it can be noted that the values of B derived from the Birch-Murnaghan equation of state for ZrN and δ-TaN are in good agreement with previously reported theoretical studies using GGA [22,23,60,61].

B. Electronic structure calculations

The electronic DOS as well as the chemical bonding between the metals and the N atoms for cubic $Zr_{1-x}Ta_xN$ solid solutions are shown in Figs. 3 and 4, where the vertical dashed line in Fig. 3 is the Fermi level (E_F). With increasing energy, the following peak manifolds can be distinguished in Fig. 3: the lowest region from -20 to -14 eV stems mainly from N $2s$ states. In the energy window from -8 to -3 eV, the N $2p$ states interact mainly with the Zr $4d$ and/or Ta $5d$ states. This strong hybridization is at the origin of the

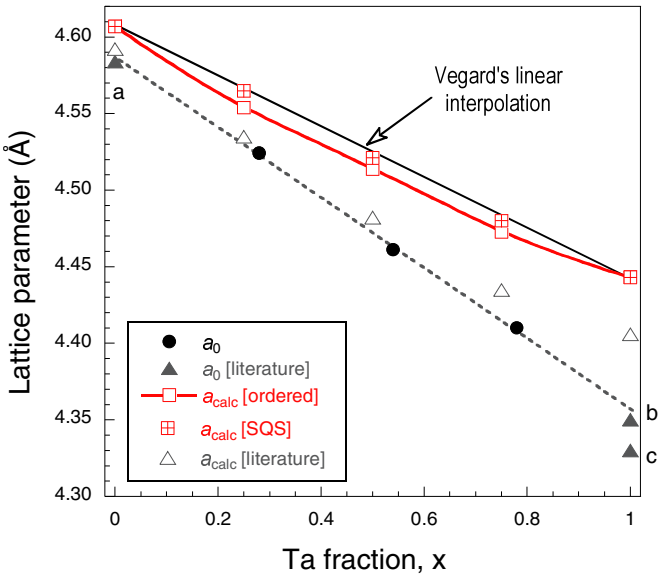

FIG. 2. (Color online) Evolution of the lattice parameter of $Zr_{1-x}Ta_xN$ alloys as a function of Ta fraction x. Open symbols refer to calculated values (a_{calc}), while filled symbols denote experimental values (a_0). For binary nitride thin films, experimental data taken from the literature are also reported for comparison. ([a]Ref. [57], [b]Ref. [28], and [c]Ref. [29]).

covalentlike bonding in these materials. The region between ~ -3 and 0 eV, referred to as the metallic region, represents the interaction between the transition metal d orbitals (t_{2g}), which are responsible for the metallic character of $Zr_{1-x}Ta_xN$. The data show that Ta alloying introduces splitting of the peak above the Fermi level compared to the parent compound; see Fig. 3. Moreover, the TaN DOS suggests a significant number of states at the Fermi level, which are dominated by the Ta $5d$ orbitals. We expect a strong Ta−N covalent bonding nature, leading to a strengthening of the Ta−N bond with respect to Zr−N. A difference in chemical bonding occurs between TaN and ZrN and is responsible for the significant difference of their elastic properties. In particular, most of the elastic constants of TaN are greater than ZrN (see Sec. IV.D). The charge density distribution and charge density difference maps in the (100) plane are presented in Figs. 4(a) and 4(b), respectively. The charge density difference is calculated by substracting the electron density of metal and N atoms rigidly separated in the geometry they have in the nitride alloys from the total electron density of ZrTaN alloys. In the case of ZrN, the Zr-N bonds have a strong ionic character as well as a covalent nature due to the interaction between Zr d and N p orbitals. Note that increasing the amount of Ta in $Zr_{1-x}Ta_xN$ causes a strengthening of $d-d$ interaction [manifested by the pronounced contours in their neighborhood, see Fig. 4(a)]. For $Zr_{0.50}Ta_{0.50}N$, the N p electrons form directional bonding with the Zr d electrons as well as with the Ta d states. The Zr d electrons of the $Zr_{0.25}Ta_{0.75}N$ compound are hybridized with the N p electrons, while the Ta electrons exhibit directional preference toward the N p electrons. This effect is more pronounced in the δ-TaN compound. Moreover, the charge density difference map also shows that the ionic bonding character is reflected mainly by the charge accumulation on

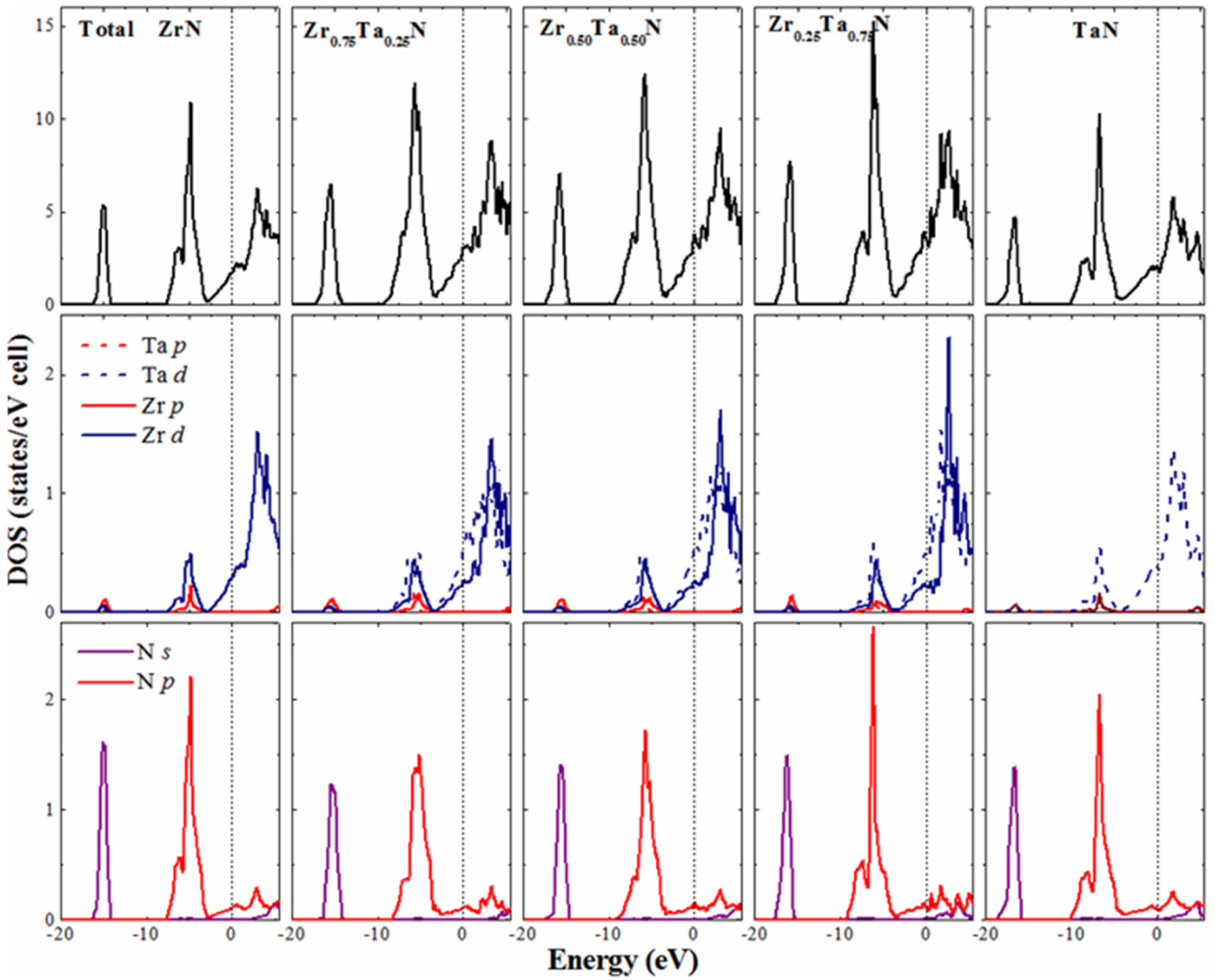

FIG. 3. (Color online) Total and partial DOS of cubic $Zr_{1-x}Ta_xN$ alloys with $x = 0$, 0.25, 0.5, 0.75, and 1. The vertical dashed line denotes the Fermi level.

the N sites [Fig. 4(b)]. Additionally, the contours indicate a charge accumulation in the middle of the Zr–N bonds as well as Ta–N. Note also that the charge density difference map indicates a clear promotion of the metallic bonds by addition of Ta. Therefore, our results demonstrate that the bonding nature of $Zr_{1-x}Ta_xN$ is characterized by a mixed covalent-ionic character that preserves the metallic features.

C. Phase composition, structure, and thermal stability of $Zr_{1-x}Ta_xN$ thin films

A representative XRR scan acquired on a ~50-nm-thick $Zr_{0.49}Ta_{0.51}N$ film is shown in Fig. 5 together with the best-fit simulation. Distinct Kiessig's fringes, extending up to more than 4° in 2θ, are observed, attesting to the relatively low surface roughness ζ of these films. The best fit of the optical model to the experimental data yields a mass density $\rho \sim 11.3$ g/cm^3, $\zeta < 1.0$ nm, and total film thickness $h = 59.1$ nm, including a topmost oxidized layer of ~3 nm. The variation of ρ with Ta fraction is reported in Table I for the $Zr_{1-x}Ta_xN$ films investigated and agrees fairly well (within 5% difference) with *ab initio* calculations reported in Table II. This suggests that these sputter-deposited films are relatively dense, despite their columnar growth morphology, as shown in Fig. 6(b). The value of $\rho = 14.3$ g.cm^{-3} obtained for the binary TaN sputtered film is consistent with that reported previously for pulsed laser deposited, highly textured δ-TaN films [29]. It is however lower than that of bulk reference powder ($\rho_{\delta-TaN} = 15.84$ g.cm^{-3}), which may be explained by the presence of a small fraction of voids (intercolumnar porosity) and possible deviation from a stoichiometric 1:1 (metal/N) ratio (see Table I). It could also indicate the presence of a hexagonal phase, as the mass density of ε-TaN is $\rho = 14.3$ g.cm^{-3}.

Figure 6(a) shows the evolution of XRD patterns for a series of ~300-nm-thick $Zr_{1-x}Ta_xN$ films with increasing Ta content. For $0 \leqslant x \leqslant 0.51$, two main XRD lines are observed around $2\theta = 34.0°$ and 39.5° and correspond to the 111 and 200 reflections of a cubic rocksalt structure (B1-type). For $x = 0.78$, the intensity of the 111 reflection is no longer visible; instead a broad and intense line is found around 40.5°, with a pronounced shoulder around 36.5°. For $x = 1$, a broad and asymmetric reflection is observed around 34.5°, a position that

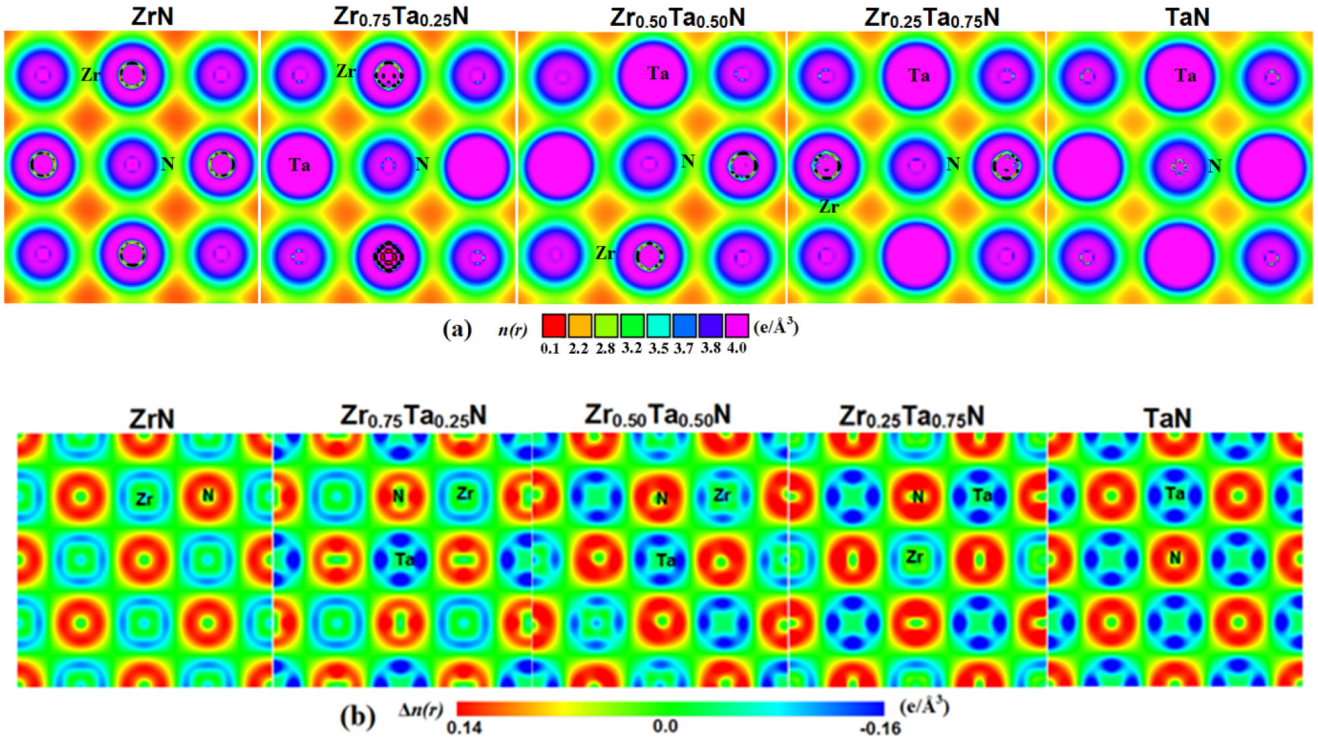

FIG. 4. (Color online) (a) Charge density distribution and (b) Charge density difference maps in the (100) plane of cubic $Zr_{1-x}Ta_xN$ alloys.

is close to the $(11\bar{2}0)$ reflection of the hexagonal ε-TaN phase. To satisfactorily reproduce peak asymmetry, the XRD line profiles of films with $x \geqslant 0.51$ were fitted with contributions from cubic δ-TaN and hexagonal ε-TaN and γ-Ta_2N phases. This fitting procedure was used for phase identification and confirms the tendency to form hexagonal phases for TaN-rich films, in good agreement with our theoretical predictions (Fig. 1).

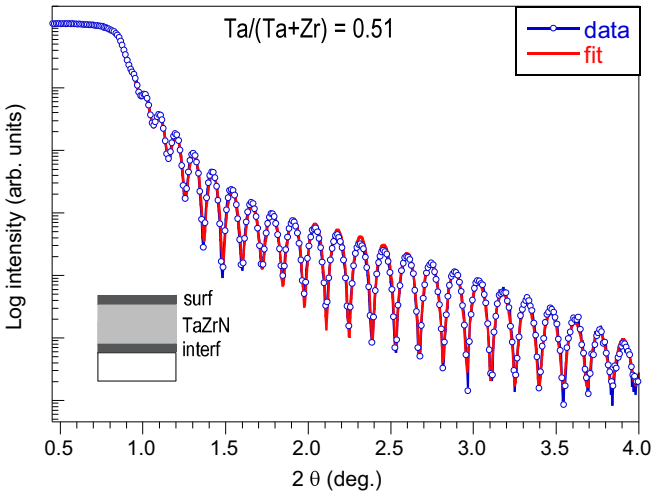

FIG. 5. (Color online) A representative XRR scan of a ~50-nm-thick magnetron sputtered $Zr_{0.49}Ta_{0.51}N$ film (open blue symbols) together with best-fit scan (red line) obtained using Parratt's formalism. The inset shows the three-layer model used for the calculations.

The phase composition of Ta-rich films ($x \geqslant 0.78$) was found to be extremely sensitive to deposition conditions, in particular to the total working pressure P_{tot} and N_2 partial pressure [51]. Several phases can be stabilized in the Ta-N system, depending on the deposition conditions [66]. Noda *et al.* [67] have shown that the nucleation and growth processes of a given crystalline phase depend critically on the film thickness and N_2/Ar gas flow ratio. In a previous paper, we have reported that single-phase cubic δ-TaN films could be successfully obtained at a higher working pressure [17] but with reduced mechanical properties [64]. Since the purpose of this paper is to explore the possibility of designing hard and tough TMN via alloying effect, we will not consider in the discussion the influence of process-dependent parameters. Note also that a gradual shift of cubic XRD lines towards higher 2θ angles occurs with increasing Ta content, which may suggest a decrease in the lattice cell size upon incorporation of Ta in the ZrN lattice. Since the angular position of XRD lines is also affected by the stress state, it is necessary to extract the *stress-free lattice parameter* a_0 to obtain information on the composition dependence of the lattice cell size. This requires a complete strain-stress state analysis, which will be reported and discussed in Sec. IV.D for selected $Zr_{1-x}Ta_xN$ films.

A closer inspection of the film with $x = 0.51$ reveals a higher background intensity level in the 36–38° angular region compared to that of films with lower Ta fractions [see Fig. 6(a)]. This is exemplified in Fig. 6(c), which displays a series of XRD patterns recorded on $Zr_{0.49}Ta_{0.51}N$ films with increasing film thickness h_f: a scattered signal, whose intensity increases with h_f, is visible between the 111 and 200 XRD lines. The presence of minor hexagonal phases, ε-TaN and γ-Ta_2N, whose main reflections are located at 34.5°, 36.7°, and 38.7°,

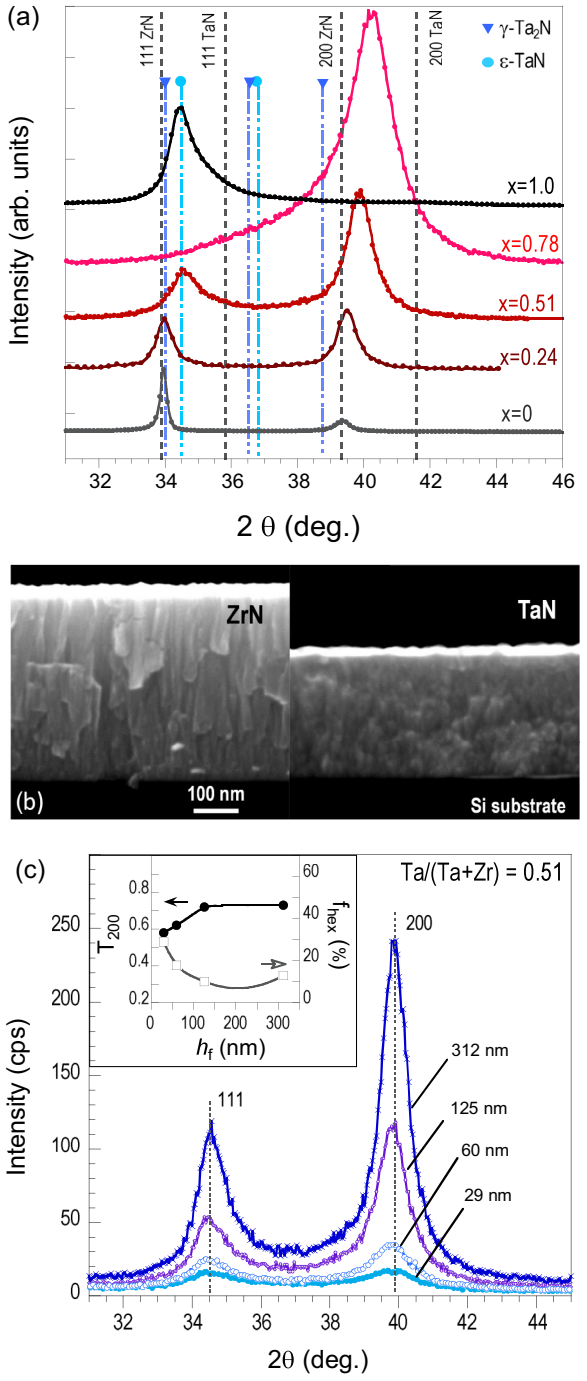

FIG. 6. (Color online) (a) Evolution of XRD patterns of ~300-nm-thick magnetron sputtered $Zr_{1-x}Ta_xN$ films with Ta fraction x. The corresponding angular positions for binary cubic ZrN and δ-TaN compounds are indicated by vertical dashed lines, together with those for hexagonal ε-TaN and γ-Ta_2N phases. (b) Cross-sectional SEM micrographs of ZrN (left) and TaN (right) films. (c) Evolution of XRD patterns of magnetron sputtered $Zr_{0.49}Ta_{0.51}N$ films as a function of film thickness h_f. The inset shows the evolution of the (200) texture coefficient, $T_{200} = I_{200}/(I_{200} + I_{111})$, where I_{200} and I_{111} are the integrated intensities of 111 and 200 cubic lines, as well as the volume fraction of hexagonal phases f_{hex} with increasing film thickness.

respectively, may be a plausible source of diffracted intensity in this region. Three contributions, the main cubic 111 and 200 lines and a broad hexagonal line centered around 37°, were used to reproduce both peak profile and background shape. The minor contribution at 37° may reflect the presence of a nanocrystalline/highly disordered hexagonal phase, similar to what has been reported for Ti-Zr-Al-N films [68]. As shown in the inset of Fig. 6(c), the fraction of the hexagonal phase is ~30% at low film thickness ($h \sim 50$ nm) and decreases to ~10% for $h_f > 100$ nm. This suggests that nucleation of cubic crystallites takes place above a critical film thickness, as reported by Noda *et al.* [67] for magnetron sputtered TaN films. Another plausible scenario would be related to the formation of a nanocomposite structure with the presence of an interfacial highly disordered tissue phase around cubic δ-TaN grains, as reported for Ti-Si-N [2,19,69] or Ti-Zr-Al-N [68] systems. Note that for ZrN-rich films ($x < 0.51$), the intensity profiles are simply the convolution of the 111 and 200 cubic lines, making these films have a single-phase cubic structure.

Along with alteration of phase composition, changes in film preferred orientation and film morphology are also revealed upon Ta alloying in ZrN. As shown in Fig. 6(a), the preferred orientation evolves from (111) at $x = 0$ to (200) at $x = 0.51$. Concomitantly, the peak width is found to increase significantly. Similar variations were also reported when increasing the Ta content in magnetron sputtered $Ti_{1-x}Ta_xN$ films deposited at the same Ar pressure [17] and attributed to the increasing energy of the deposited flux [70,71]. As calculated using the Stopping and Range of Ions in Matter (SRIM) computer code [72], Ta sputtered atoms are more energetic compared to Ti ones; also a higher backscattering yield of Ar is obtained when sputtering a Ta target compared with a Ti one ($M_{Ta} > M_{Ti} > M_{Ar}$), which leads to a larger flux of energetic backscattered neutrals with increasing Ta atoms flux. Both sputtered atoms and backscattered Ar particles transfer their energy to the growing film, increasing adatom mobility but also creating defects and impurities deeper in the layer that contribute to the disruption of the preferential (111) columnar growth. This results in a finer-grained (nanocrystalline) structure with (200) preferred orientation and increased compressive stress [71]. Based on the present findings [Fig. 6(a)], the same scenario is likely to take place in the ZrTaN system when substituting Ta for Zr. Scanning electron microscopy observations on cross-sectional $Zr_{1-x}Ta_xN$ samples confirm this densification with increasing x [Fig. 6(b)].

Figure 7 shows the evolution of XRD patterns of ternary films after vacuum annealing at 850 °C for 3 h. The same Bragg reflections are evidenced in the as-grown and annealed states, the only minor modification being a change in peak position. A shift towards larger 2θ angles is indeed systematically observed after annealing, being more pronounced for the 200 line. This implies a reduction in the out-of-plane lattice parameter. The results of the strain analysis reported in Sec. IV.D show that this structural change is related to a significant relaxation of the growth-induced compressive stress, similarly to what has been reported for magnetron sputtered Ti-Zr-N [14,71] and Ti-Ta-N films [71]. Apart from this, the results of Fig. 7 clearly demonstrate that $Zr_{1-x}Ta_xN$ films are thermally stable up to 850 °C, despite the driving force towards phase separation discussed in Sec. IV.A from ground state energy considerations.

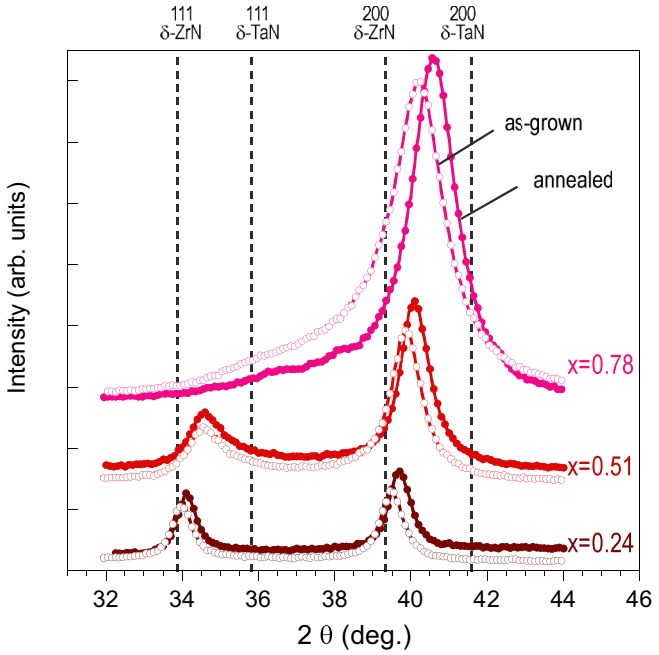

FIG. 7. (Color online) Comparison of XRD patterns of ∼300-nm-thick magnetron sputtered $Zr_{1-x}Ta_xN$ films before (open symbols) and after thermal annealing at 850 °C for 3 h under vacuum (filled symbols).

D. Stress: *in situ* wafer curvature and *ex situ* x-ray diffraction

The intrinsic stress evolution measured in real time during sputter deposition of various $Zr_{1-x}Ta_xN$ films is shown in Fig. 8(a), where the quantity $\sigma_{avg} \times h_f$ is plotted against h_f. The stress is strongly compressive for all samples, with typical values in the range of −3.0 to −4.5 GPa. However, distinct behaviors are noticed with increasing film thickness h_f, depending on film composition. For low Ta contents, $x = 0$ and $x = 0.14$, the magnitude of compressive stress decreases with film thickness h_f. This is better shown in Fig. 8(b), where the average stress σ_{avg} is plotted against h_f. A maximum of ∼−4 GPa is reached at $h_f \sim 20$ nm, then σ_{avg} gradually increases. For $x = 0.24$, a steady-state compressive stress of −4.2 GPa is observed. For $x = 0.51$ and 0.78, the compressive stress is lower in the early growth stages and then increases with h_f. This is clearly shown in Fig. 8(b) for the $Zr_{0.22}Ta_{0.78}N$ film: σ_{avg} is approximately constant to −2 GPa for $h_f <$ 30 nm, then it decreases to −3 GPa at $h_f \sim 70$ nm and down to −3.6 GPa for $h_f \sim 150$ nm.

The above stress evolutions can be categorized in three distinct behaviors, according to the different growth regimes and resulting microstructures involved when increasing Ta atoms flux, i.e. increasing growth energetics, as already discussed in Sec. IV.C.

Regime I ($0 \leqslant x < 0.24$) corresponds to a typical "zone T" columnar growth regime [71,73–75] with stress gradients along the growth direction, similar to what has been reported for ZrN and TiN films deposited at high working pressures [56,76,77]. The intrinsic stress is the sum of two competing stress sources: atomic peening at the origin of defect incorporation and compressive stress, and attractive forces at the grain/column boundary at the origin of tensile

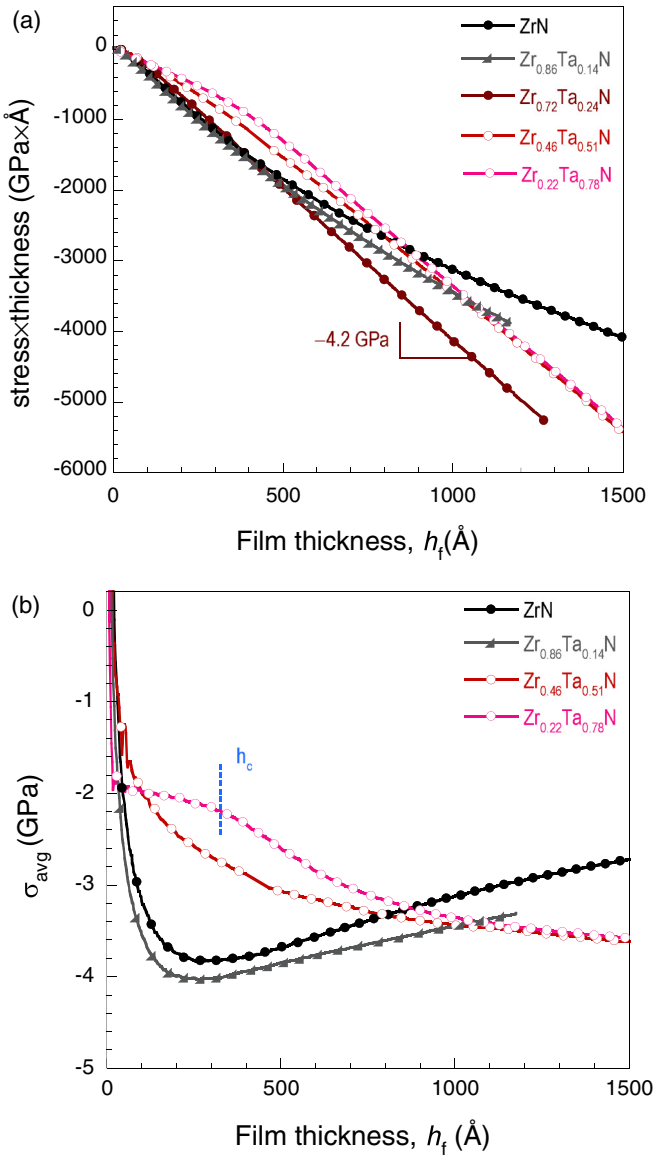

FIG. 8. (Color online) MOSS data during sputter deposition of $Zr_{1-x}Ta_xN$ films with different Ta contents (a) evolution of the stress × thickness product and (b) evolution of the average stress σ_{avg}.

stress. Compressive and tensile stress components are additive contributions to the overall intrinsic stress. Atomic peening prevails in the early growth stages ($h_f < 20$ nm), while attractive forces manifest stronger when columns start to form. Regime I is characterized by the development of a (111)-preferred orientation [see Fig. 6(a)].

Regime II ($x = 0.24$) corresponds to the development of a steady-state compressive stress regime all along deposition. The intense bombardment of the film, here provided by incoming energetic Ta atoms and backscattered Ar [70,71], favors film densification and renucleation, resulting in a finer grained morphology. This is consistent with the presence of two main grain populations, with (111) and (200) preferred orientation, as observed in Fig. 6(a).

Regime III ($0.51 \leqslant x \leqslant 0.78$) corresponds to the formation of a nanocomposite film with (200)-oriented, nanoscale cubic

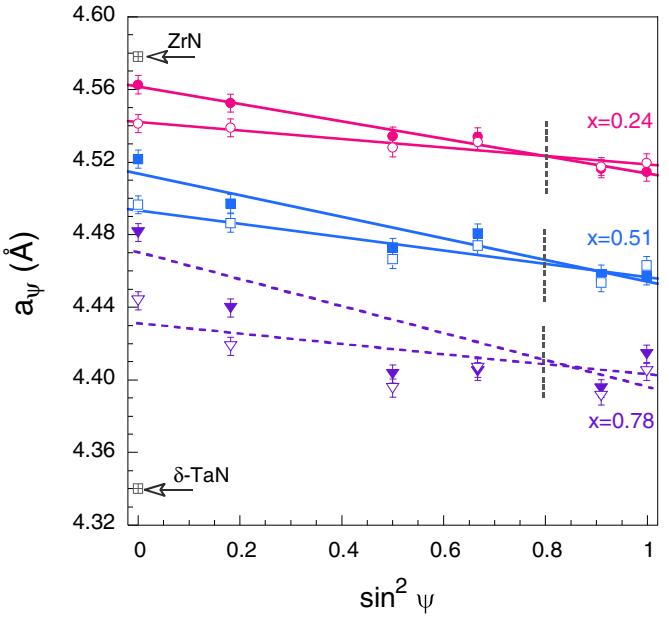

FIG. 9. (Color online) $\sin^2\psi$ plots of $Zr_{1-x}Ta_xN$ films before (filled symbols) and after vacuum annealing at 850 °C for 3 h (open symbols) for $x = 0.24$, 0.51, and 0.78. The bulk lattice parameter of ZrN and TaN reference powders is also reported. The vertical dashed line shows the intersection point ($\sin^2\psi_0 \sim 0.8$; a_0) of the $\sin^2\psi$ lines for a given alloy composition.

grains surrounded by a hexagonal interfacial phase. It is speculated that defect creation in the nanocrystalline/highly disordered hexagonal phase corresponds to a lower stress state than in cubic crystallites. As the film thickens, the fraction of hexagonal phase decreases [see Fig. 4(c)]; consequently a larger compressive stress develops, reaching eventually a steady-state regime. The stress transition observed above $h_c \sim 30$ nm for $x = 0.78$ [see Fig. 8(b)] could reflect the change in nucleation and growth rate of the cubic crystals.

The evolution of the lattice parameter a_ψ of (200)-oriented crystallites in the as-deposited and vacuum annealed states is shown in Fig. 9 as a function of $\sin^2\psi$ for three alloy compositions $x = 0.24$,0.51, and 0.78. All $Zr_{1-x}Ta_xN$ films are in a compressive stress state, as evidenced by the negative slope of the $\sin^2\psi$ lines. With increasing Ta fraction, a shift of the $\sin^2\psi$ lines towards lower a_ψ values is observed, in agreement with the evolution of the lattice parameter with x (Fig. 2). However, the shift is not constant with ψ angle, indicating different elastic strain states depending on Ta fraction. For $x = 0.78$, the evolution of a_ψ with $\sin^2\psi$ deviates from linearity, attesting to the presence of stress gradients along the film thickness. After annealing, a decrease of the slope of the $\sin^2\psi$ lines is systematically observed. This reflects a reduction of the compressive residual stress related to a relief of growth-induced defects at temperatures higher than the deposition temperature [33,71]. Interestingly, for a given alloy composition, the $\sin^2\psi$ lines in the as-deposited and annealed states are found to intersect at a similar value $\sin^2\psi_0 \sim 0.8$. From the ordinate of this intersection point, one can readily determine the stress-free lattice parameter a_0. These a_0 values were reported in Fig. 2 as a function of Ta fraction.

In order to relate the measured elastic strain obtained from *ex situ* XRD (Fig. 9) to the residual stress state of the films, knowledge of the elastic properties of the film is required. We used the set of c_{ij} elastic constants calculated from the present DFT computational approach on ordered compounds (see Table III) to derive the stress values of the $Zr_{1-x}Ta_xN$ films. We also assumed an equibiaxial stress state ($\sigma = \sigma_1 = \sigma_2$), as commonly observed in fiber-textured thin films. The obtained stress data are reported in Table I. The choice of another set of elastic constants (e.g. using SQS values) would marginally affect the extracted stress values (~10% error).

In the as-deposited state, films are under large compressive stress, ranging from −4.7 to −8.3 GPa with increasing Ta fraction. A higher uncertainty is associated with the determination of the stress in the film with $x = 0.78$ due to the larger spread of a_ψ data, especially in the as-deposited state (see Fig. 9). The stress is significantly relieved after vacuum annealing since the absolute magnitude decreases by 40–50%. Note that the absolute stress values derived from XRD cannot be directly compared to those obtained from *in situ* MOSS; however, the two techniques converge towards similar stress evolutions in $Zr_{1-x}Ta_xN$ films with chemical alloying.

E. Elastic properties

1. DFT calculations

The calculated variation of the total energy with the applied strain to induce deformation in the lattice was used to determine the elastic properties of $Zr_{1-x}Ta_xN$ alloys [78]. The details of elastic constant calculations are given in the Supplemental Material [51]. The calculated stiffness constants c_{11}, c_{12}, and c_{44} for cubic compounds (ordered supercells) and cubic-averaged elastic constants $\bar{C}_{11}$, $\bar{C}_{12}$, and $\bar{C}_{44}$ for disordered SQS alloys [46,51] (obtained from optimized lattice parameters of $Zr_{1-x}Ta_xN$ alloys) are given in Table III together with available experimental [79] and theoretical data [14,22,23,59,61,64,80–82], for binary nitrides. All the calculated c_{ij} values are satisfying the Born and Huang's [83] stability criteria for a cubic crystal, pointing therefore to mechanically stable alloy systems. For binary nitrides, our results are in general in good agreement with available data. For ZrN, relative errors of 10–20% are obtained as compared to neutron scattering measurements [79], but our calculated values respect the $c_{11} > c_{44} > c_{12}$ tendency in much better accordance than with DFT-pseudopotential calculations [14,81].

For the ordered supercells, the calculated c_{11} and c_{12} constants of $Zr_{1-x}Ta_xN$ alloys gradually increase with increasing Ta fraction, while a substantial softening of c_{44} is obtained, reaching 55% when spanning ZrN to TaN. This evolution of c_{44} suggests a higher resistance to deformation with respect to a shearing stress for TaN-rich ternary alloys. One can notice that the SQS configuration entails a strong decrease of c_{11} and increase of c_{12} and c_{44} compared to values for ordered compounds. This reflects a change in elastic anisotropy at the crystal level depending on the atomic configuration, as also reported by Tasnádi *et al.* for TiAlN (see fig. 5 of Ref. [46]). However, the $c_{ij}(x)$ trends are consistent for both supercell arrangements.

TABLE III. Calculated (calc) elastic constants c_{ij}, bulk modulus B_H, shear modulus G_H, Young's modulus E, and Poisson's ratio ν, of cubic $Zr_{1-x}Ta_xN$ alloys for ordered (bold values) and SQS disordered (marked with *) configurations. Also reported are experimental (exp) and theoretical data from the literature for binary nitrides. Note that for SQS supercells, the elastic constants correspond to projected principal cubic elastic constants $\bar{C}_{ij}$ (expressions are given in the Supplemental Material [51]).

	c_{11} (GPa)	c_{12} (GPa)	c_{44} (GPa)	$c_{12}-c_{44}$ (GPa)	B_H (GPa)	G_H (GPa)	E (GPa)	ν	G_H/B_H
ZrN	**524**	**108**	**119**	**−11**	**246**	**149**	**372**	**0.248**	**0.60**
	471[a]	88[a]	138[a]	−50	215[a]	160[a]		0.16[a]	
	523[b]	111[b]	116[b]	−5	250[b]	138[b]	350[b]		
	528[c]	95[c]	126[c]	−31	239[c]	159[c]	386[c]	0.23[c]	
	537[d]	118[d]	120[d]	−2	258[d]	145[f]	365[d]	0.16[h]	
	504[e]	116[e]	120[e]	−4	226[f]	176[h]	378[l]	0.25[l]	
	491[f]	93[f]	117[f]	−24	268[g]	151[l]			
	606[g]	99[g]	128[g]	−29	285[h]				
	611[h]	117[h]	129[h]	−12	250[l]				
	531[l]	110[l]	121[l]	−11					
$Zr_{0.75}Ta_{0.25}N$	**556**	**106**	**108**	**−2**	**256**	**146**	**368**	**0.261**	**0.57**
	433*	181*	172*	9*	265*	144*	366*	0.270*	0.54*
$Zr_{0.50}Ta_{0.50}N$	**645**	**127**	**94**	**33**	**300**	**143**	**370**	**0.294**	**0.48**
	443*	197*	159*	38*	278*	137*	353*	0.288*	0.49*
$Zr_{0.25}Ta_{0.75}N$	**668**	**124**	**82**	**42**	**305**	**136**	**355**	**0.307**	**0.44**
	447*	217*	154*	63*	293*	127*	333*	0.310*	0.44*
TaN	**726**	**133**	**66**	**67**	**330**	**127**	**337**	**0.330**	**0.38**
	715[b]	138[b]	60[b]	78[b]	325[b]	110[b]	300[b]		
	881[i]	122[i]	74[i]	48[i]	375[i]	153[i]	404[i]	0.32[k]	
	827[j]	156[j]	73[j]	83[j]	373[k]	143[k]	380[j]	0.329[k]	
	901[k]	109[k]	72[k]	37[k]	333[l]	119[l]	381[k]	0.34[l]	
	699[l]	149[l]	62[l]	87[l]			318[l]		

[a]Reference [79]; exp.
[b]Reference [22]; calc GGA.
[c]Reference [80]; calc GGA.
[d]Reference [81]; calc GGA.
[e]Reference [14]; calc GGA.
[f]Reference [82]; calc GGA.
[g]Reference [82]; calc LDA.
[h]Reference [79]; calc LDA.
[i]Reference [61]; calc GGA.
[j]Reference [69]; calc LDA.
[k]Reference [64]; calc GGA.
[l]Reference [23]; calc GGA.

It has been suggested in the literature [20–24] that a negative Cauchy pressure $c_{12}-c_{44}<0$ corresponds to more directional bonding, while positive values indicate predominant metallic bonding. Indeed, the calculated Cauchy pressure is slightly negative for ZrN for which a smaller charge transfer from cation to anion takes place. Cauchy pressure increases to positive values with increasing Ta concentration in the ZrN lattice, i.e. with higher VEC, as these electrons contribute mainly to the metal-metal d-d interactions [22].

The polycrystalline isotropic elastic moduli B_H, G_H, and E were calculated assuming a Hill average [53] of the single-crystal elastic constants c_{ij}. These are reported in Table III for the ordered and SQS supercell configurations (see Ref. [51] for corresponding expressions). From this table, one can see that the values of B_H agree with those derived from the Birch-Murnaghan equation of state (Table II). Our calculated value of the ZrN bulk modulus $B_H = 246$ GPa is overestimated by around 15% with respect to the experimental data obtained from the neutron scattering measurements [79]. The calculated value of the ZrN shear modulus $G_H = 149$ GPa is in agreement with the previously reported theoretical [22,59,80–82] and experimental data [79]. For δ-TaN, our calculated values are also consistent with available literature data [22,23,59,61,64], although reported values are more spread. We obtain a close agreement with the recent calculations of Holec *et al.* [22], who used the same PAW-GGA formalism. We also remark that the shear and Young's modulus of ZrN are higher than those of TaN. The larger shear modulus of ZrN is mainly due to its larger c_{44} constant.

Figure 10(a) shows the calculated bulk moduli, shear moduli, and Young's moduli of $Zr_{1-x}Ta_xN$ alloys with different supercell arrangements (ordered and SQS) as a function of the Ta concentration, as well as the measured indentation moduli obtained in this paper (see Supplemental Material, Ref. [51]). Our results for ordered and SQS supercells are consistent with each other despite distinct magnitudes of c_{ij}. They both show that an increase in Ta content leads to an increase in bulk modulus and decrease of the shear and Young's moduli.

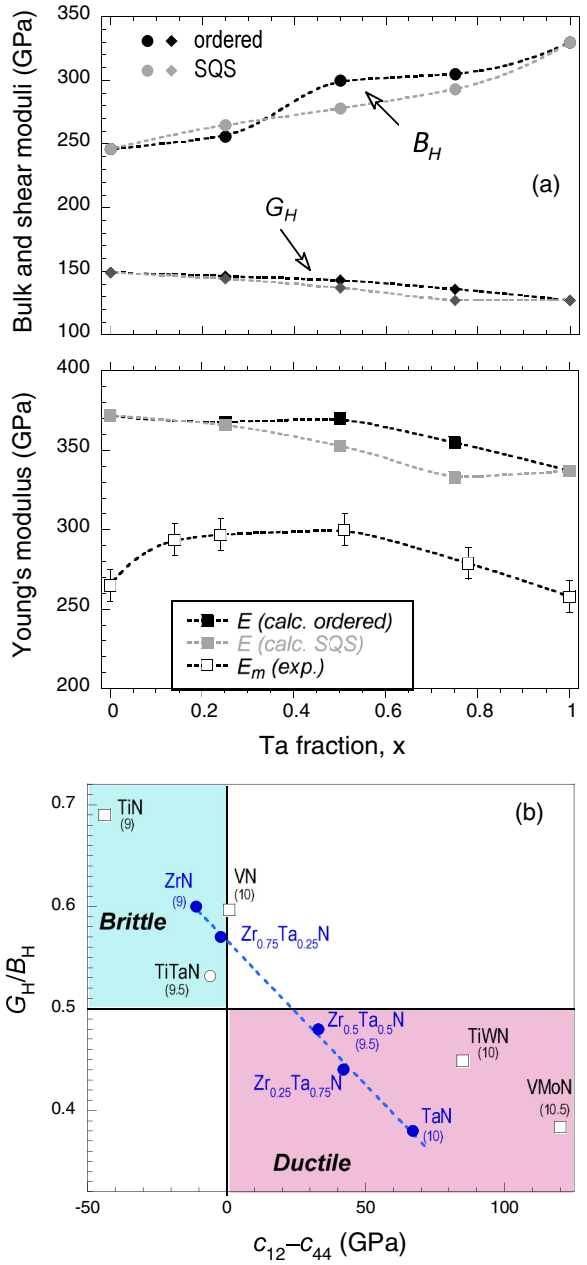

FIG. 10. (Color online) (a) Calculated bulk modulus B_H (circles), shear modulus G_H (diamonds), and Young's modulus E (filled squares) of $Zr_{1-x}Ta_xN$ alloys as a function of Ta fraction x. The measured elastic modulus E_m from nanoindentation is also reported (open squares). (b) Brittleness vs ductility map of the $Zr_{1-x}Ta_xN$ compounds as estimated in this work (filled circles), and compared to other binary or ternary TMN from the literature (open symbols) [11,12,64]. Numbers in parentheses indicate the number of VEC.

This behavior is the opposite of that observed in $Zr_{1-x}Ti_xN$ alloys [14]. The calculated Young's moduli are overestimated by ~20–30% with respect to the experimental values obtained from nanoindentation on thin films. Similar trends were also observed in transition metal diborides [84]. Nevertheless, the agreement between our calculations and the experiments is still satisfactory, compared to previous work by Aouadi [10] where deviations as large as 80% were obtained.

Poisson's ratio can formally take values between −1 and 0.5, which correspond, respectively, to the lower bound where the material does not change its shape and to the upper bound when the volume remains unchanged. The value of the Poisson's ratio ν for covalent materials is small ($\nu \sim 0.1$), whereas for ionic materials, a typical value of ν is 0.25 [85]. Our calculated Poisson's ratio values (ordered and SQS supercells) vary between 0.25 and 0.33, which means that $Zr_{1-x}Ta_xN$ solid solutions are affected by a certain amount of ionic contributions. Based on an evaluation of a large experimental dataset, Pugh [20] proposed that low G/B values, i.e. < 0.571, are associated with ductility, while higher values indicate brittleness. In our case, according to this indicator (Table III), $Zr_{1-x}Ta_xN$ alloys are expected to behave essentially as brittle materials. However, the addition of Ta above $x \sim 0.5$ induces a decisively ductile character in ZrN. In Fig 10(b), we map out the brittleness vs ductility behavior of all the $Zr_{1-x}Ta_xN$ compounds using the Pugh [20] and Pettifor [24] criteria. It can be seen that the addition of Ta induces an important ductile character in the clearly brittle ZrN. The results of Fig. 10(b) confirm the elastic trends reported by Sangiovanni *et al.* [11,12] and Kindlund *et al.* [21] for other ternary TMN alloys, that is, supertoughening can be achieved in these class of materials by fine-tuning the VEC through alloying. For the Zr-Ta-N system, the origin of enhanced toughness with increased Ta content can be related to the more pronounced covalent character of metal-N bonds, combined with increased metallic bonding between Zr and Ta, as the presence of Ta delocalizes more charge in the regions between the nuclei [see Figs. 4(a) and 4(b)].

2. *Experimental determination*

The Rayleigh wave velocity is one of the most useful pieces of information among the raw data obtained in the BLS experiment for thick opaque films on a substrate as it is closely related to the transverse velocity ($V_R = \beta V_T$) and thus to the shear elastic constant ($C_{44} = \rho V_T^2$). The variation of V_R is shown in Fig. 11 and exhibits a large decrease and a nearly linear dependence as a function of Ta concentration as long as the rocksalt structure is ensured ($x \leqslant 0.78$). The same observation was revealed for single-phase, cubic $Ti_{1-x}Zr_xN$ alloy thin films [14]. However, for ternary $Ti_xTa_{1-x}N$ thin films [64], deviation from this linear behavior was observed for the TaN film deposited at low Ar pressure (0.5 Pa) in relation to its peculiar microstructural state: the presence of a mixture of cubic (δ-TaN) and hexagonal phases (ε-TaN and γ-Ta_2N) led to a significant hardening compared to linear interpolation. A similar trend is obtained here for $x > 0.78$ in $Zr_{1-x}Ta_xN$ films (region III of Fig. 11), which, based on XRD results of Fig. 4(a), points towards the same microstructural origin.

The shear elastic constant C_{44} of the $Zr_{1-x}Ta_xN$ thin films was calculated from the V_R values reported in Table IV using a β parameter of ~0.9–0.97, as determined from the fit of the BLS spectra, and mass density values reported in Table I. Our β parameter remains close to the common value ≈0.94 [37] that was found for many materials, indicating a reliable fitted C_{44} value (uncertainty below 8%). The evolution of C_{44} with Ta content x is shown in Fig. 12. The observed softening of V_R and V_T (Fig. 11) is greatly counterbalanced by the

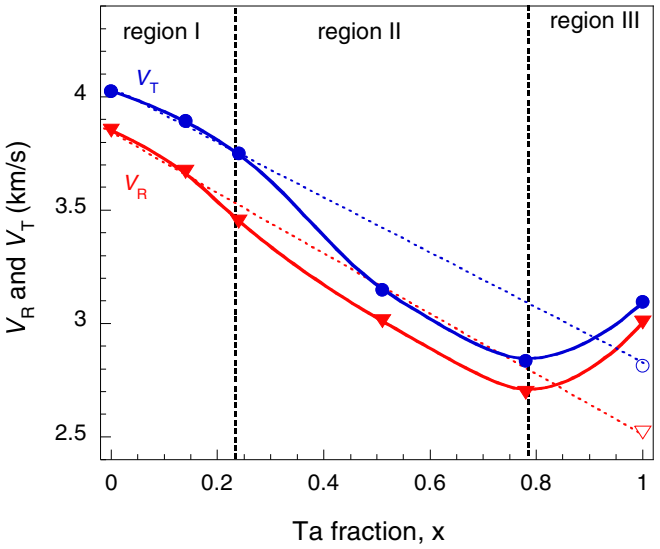

FIG. 11. (Color online) Rayleigh surface wave velocity V_R (triangles) and transverse velocity V_T (circles) measured from BLS experiments as a function of Ta fraction x. Filled symbols refer to Ar working pressure of 0.3 Pa (this paper) whereas open symbols correspond to the values for a single-phase, cubic δ-TaN film deposited at 1.0 Pa [64].

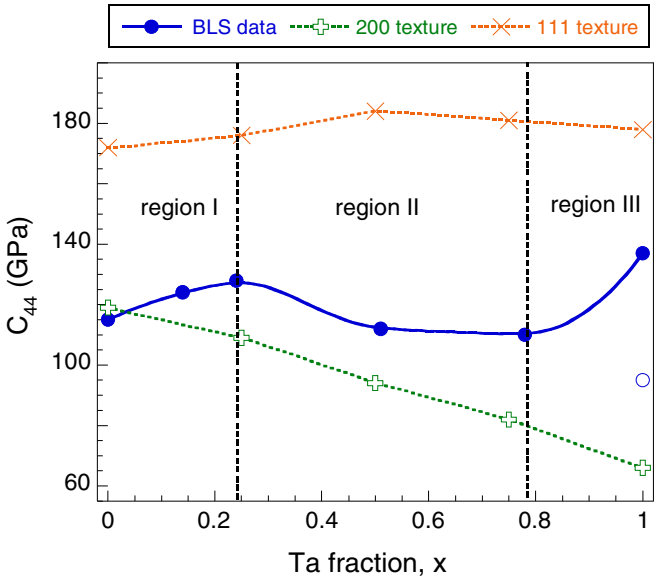

FIG. 12. (Color online) Shear elastic constant C_{44} measured from BLS experiments (filled symbols) as a function of Ta fraction x. Crosses correspond to calculated effective $\langle C_{44}\rangle$ values assuming a (111) or (200) texture. Filled symbols refer to Ar working pressure of 0.3 Pa (this paper), whereas the open circle refers to a δ-TaN film deposited at 1.0 Pa [64].

large ($\sim$50%) increase in ρ (see Table I) and thus does not reflect in a direct way the complex evolution of the shear elastic constant with x. As seen in Fig. 12, three regions can be distinguished as a function of Ta content. C_{44} increases from 115 to 128 GPa for $0 \leqslant x \leqslant 0.24$ (region I) and then decreases to $\sim$110 GPa for $0.24 < x \leqslant 0.78$ (region II). It increases again if we consider the TaN film (region III), which exhibits a mixture of cubic and hexagonal phases [see Fig. 4(a)]. A similar, though more pronounced, behavior was observed by Aouadi [10] for the hardness H and the elastic modulus E_{exp} evolutions, as derived from nanoindentation tests on magnetron sputtered $Zr_{1-x}Ta_xN$ films. The maximum hardness (37 GPa) peaked at a Ta concentration $x \sim 0.30$. This coincides with the maximum value of 128 GPa derived in this paper for the shear elastic constant C_{44}. However, we obtain a different hardness evolution [51]. Two main reasons were proposed by Aouadi to explain this nonmonotonous behavior:

TABLE IV. Experimental Rayleigh wave velocity V_R, shear elastic constant C_{44}, and β parameter obtained from BLS of 300-nm-thick $Zr_{1-x}Ta_xN$ thin films.

Ta fraction	V_R (m/s)	β	C_{44} (GPa)
0	3850	0.956	115
0	3980[a]	0.942[a]	132[a]
0.14	3670	0.930	124
0.24	3450	0.919	128
0.51	3010	0.956	112
0.78	2695	0.951	110
1.0	3005	0.970	137
1.0	2520[b]	0.895[b]	95[b]

[a]At 0.19 Pa working pressure, Ref. [14].
[b]At 1.0 Pa working pressure, Ref. [64].

(i) a solid solution hardening since the replacement of Zr by Ta atoms can cause lattice distortion, and the resulting stress field can interact with the elastic stress field of dislocations; (ii) a limited segregation of solute atoms at grain boundaries, which could be created by the energetic species that bombard the film during the sputtering process. In this paper, a solid solution hardening effect is expected to take place for films with $0 \leqslant x \leqslant 0.24$, i.e. corresponding to regime I, as these films possess a single-phase, cubic $Zr_{1-x}Ta_xN$ structure [Fig. 4(a)]. The second mechanism is also plausible in the present deposition conditions as discussed before: the formation of a dense, fine-grained nanocomposite structure is evidenced for TaN-rich films, with the presence of an interfacial hexagonal tissue around cubic δ-TaN grains, similar to what is observed in the Ti-Si-N system [2,19]. At the same time, the $Zr_{1-x}Ta_xN$ films undergo a texture evolution from (111) to (200) with increasing Ta fraction [Fig. 4(a)]. For strong anisotropic materials like the $Zr_{1-x}Ta_xN$ films considered here, the preferred orientation of crystallites should have a significant impact on their elastic response. To account for this possible contribution, we have calculated the polycrystalline Hill averaged [53] effective elastic constants $\langle C_{ij}\rangle$ for the (111) and (200) textures, as well as for the case of a random orientation of the crystallites. These $\langle C_{ij}\rangle$ values are reported in Table V. They experience opposite behavior with the alloy composition when considering either a (111) or (200) texture. For the shear elastic constant, a strong decrease in $\langle C_{44}\rangle$ is obtained for the (200) texture when increasing the Ta fraction, while the assumption of a (111) texture would result in little evolution in $\langle C_{44}\rangle$ (see Fig. 12). These results can partly explain the decrease in C_{44} (region II) of $Zr_{1-x}Ta_xN$ films with $x = 0.51$ and 0.78 having a (200) preferred orientation [Fig. 4(a)]. Deviation from stoichiometry

TABLE V. Calculated effective elastic constants $\langle C_{11}\rangle$, $\langle C_{33}\rangle$, $\langle C_{13}\rangle$, $\langle C_{12}\rangle$, and $\langle C_{44}\rangle$ (in GPa) of the polycrystalline $Zr_{1-x}Ta_xN$ alloys using the Hill average [53] and considering different preferred orientation of the crystallites.

Film composition	$\langle C_{11}\rangle$	$\langle C_{33}\rangle$	$\langle C_{13}\rangle$	$\langle C_{12}\rangle$	$\langle C_{44}\rangle$	Texture
ZrN	445	445	147	147	149	None
	429	405	167	143	172	{111}
	473	524	108	159	119	{002}
$Zr_{0.75}Ta_{0.25}N$	432	401	184	153	176	{111}
	488	556	106	175	109	{002}
$Zr_{0.5}Ta_{0.5}N$	465	425	237	197	184	{111}
	543	645	127	229	94	{002}
$Zr_{0.25}Ta_{0.75}N$	459	415	251	207	181	{111}
	547	668	124	245	82	{002}
TaN	468	418	287	237	178	{111}
	574	726	133	285	66	{002}

may also affect the shear elastic modulus values of $Zr_{1-x}Ta_xN$ films. For understoichiometric TiN_x compounds, Jhi *et al.* [86] and Shin *et al.* [87] reported a softening of shear and Young's moduli, respectively. It was argued that the presence of N vacancies increases the occupied metallic *d-d* bonding states near the Fermi level, at the origin of decreasing G values.

V. CONCLUSIONS

We employed *ab initio* calculations and thin-film growth experiments to obtain a comprehensive picture on the structural, electronic, and mechanical properties of ternary Ta-Zr-N alloys. Both ordered and disordered metal configurations were considered on the cation sublattice for modeling the structural and elastic properties of ternary $Zr_{1-x}Ta_xN$ compounds. The results show that Ta alloying in cubic ZrN lattice induces significant toughness enhancement while retaining a high hardness (>30 GPa). The improvement of the mechanical properties of ternary $Zr_{1-x}Ta_xN$ thin films stems from the increased valence electron concentration, which influences chemical bonding, and the existence a mixture of cubic and hexagonal phases, which influences phase stability, when Ta substitutes for Zr.

Our DFT electronic band structure calculations using a GGA scheme reveal a strong delocalization of the *d* states of the transition metal ions and *2p* states of N, in addition to ionic and metallic features. The strong hybridization character has an important effect on the elastic behavior of these alloys. The elastic constants, bulk modulus and its pressure derivative, as well as polycrystalline Young's and shear moduli, and Poisson ratio have been calculated. A significant decrease of the G_H/B_H ratio is predicted, from 0.60 to 0.38, with increasing Ta fraction, which confers to TaN-rich alloys a ductile behavior.

Experimentally, the evolution of the shear modulus (= C_{44} elastic constant), as determined from Brillouin light scattering experiments, is rather complex. We ascribe the observed nonmonotonous evolution with Ta fraction to a change in texture and phase formation as a result of the increased deposited energy. This is accompanied by film densification, with disruption of columnar growth, as well as the creation of defects at the origin of the relatively large compressive stress (>4 GPa). Nanoindentation tests on as-deposited and vacuum annealed ternary samples show that the increased hardness (42% with respect to the rule of mixture) has intrinsic origin (fine-grain morphology, solid solution hardening). Finally, $Zr_{1-x}Ta_xN$ coatings with $x = 0.51$ and $x = 0.78$ exhibit hardness over Young's modulus ratios $H/E > 0.1$, which makes them potential candidates for wear-resistant applications.

[1] W. D. Sproul, Science **273**, 889 (1996).
[2] S. Veprek and M. J. G Veprek-Heijman, Surf. Coat. Technol. **202**, 5063 (2008).
[3] G. M. Matenoglou, L. E. Koutsokeras, and P. Patsalas, Appl. Phys. Lett. **94**, 152108 (2009).
[4] T. Seppänen, L. Hultman, and J. Birch, Appl. Phys. Lett. **89**, 181928 (2006).
[5] L. E. Koutsokeras, G. Abadias, Ch. E. Lekka, G. M. Matenoglou, D. F. Anagnostopoulos, G. A. Evangelakis, and P. Patsalas, Appl. Phys. Lett. **93**, 011904 (2008).
[6] H. Holleck, J. Vac. Sci. Technol. A **4**, 2661 (1986).
[7] P. H. Mayrhofer, C. Mitterer, L. Hultman, and H. Clemens, Progr. Mater. Sci. **51**, 1032 (2006).
[8] L. Hultman, J. Bareño, A. Flink, H. Söderberg, K. Larsson, V. Petrova, M. Odén, J. E. Greene, and I. Petrov, Phys. Rev. B **75**, 155437 (2007).
[9] T. Joelsson, L. Hultman, H. W. Hugosson, and J. M. Molina-Aldareguia, Appl. Phys. Lett. **86**, 131922 (2005).
[10] S. M. Aouadi, J. Appl. Phys. **99**, 053507 (2006).
[11] D. G. Sangiovanni, V. Chirita, and L. Hultman, Phys. Rev. B **81**, 104107 (2010).
[12] D. G. Sangiovanni, L. Hultman, and V. Chirita, Acta Mater. **59**, 2121 (2011).
[13] H. Lind, R. Forsén, B. Alling, N. Ghafoor, F. Tasnádi, M. P. Johansson, I. A. Abrikosov, and M. Odén, Appl. Phys. Lett. **99**, 091903 (2011).
[14] G. Abadias, V. I. Ivashchenko, L. Belliard, and Ph. Djemia, Acta Mater. **60**, 5601 (2012).
[15] P. Patsalas, G. Abadias, G. M. Matenoglou, L. E.Koutsokeras, and Ch. E. Lekka, Surf. Coat. Technol. **205**, 1324 (2010).
[16] G. M. Matenoglou, L. E. Koutsokeras, Ch. E. Lekka, G. Abadias, C. Kosmidis, G. A. Evangelakis, and P. Patsalas, Surf. Coat. Technol. **204**, 911 (2009).
[17] G. Abadias, L. E. Koutsokeras, S. N. Dub, G. N. Tolmachova, A. Debelle, T. Sauvage, and P. Villechaise, J. Vac. Sci. Technol. A **28**, 541 (2010).
[18] L. E. Koutsokeras, G. Abadias, and P. Patsalas, J. Appl. Phys. **110**, 043535 (2011).
[19] S. Hao, B. Delley, S. Veprek, and C. Stampfl, Phys. Rev. Lett. **97**, 086102 (2006).
[20] S. F. Pugh, Phil. Mag. **45**, 823 (1954).

[21] H. Kindlund, D. G. Sangiovanni, L. Martinez-de-Olcoz, J. Lu, J. Jensen, J. Birch, I. Petrov, J. E. Greene, V. Chirita, and L. Hultman, APL Materials **1**, 042104 (2013).

[22] D. Holec, M. Friàk, J. Neugebauer, and P. H. Mayrhofer, Phys. Rev. B **85**, 064101 (2012).

[23] V. Petrman and J. Houska, J. Mater. Sci. **48**, 7642 (2013).

[24] D. G. Pettifor, Mater. Sci. Technol. **8**, 345 (1992).

[25] K. Chen, L. R. Zhao, J. Rodgers, and J. S. Tse, J. Phys. D: Appl. Phys. **36**, 2725 (2003).

[26] D. G. Sangiovanni, V. Chirita, and L. Hultman, Thin Solid Films **520**, 4080 (2012).

[27] S. M. Aouadi, P. Filip, and M. Debessai, Surf. Coat. Technol. **187**, 177 (2004).

[28] C.-S. Shin, D. Gall, Y.-W. Kim, N. Hellgren, I. Petrov, and J. E. Greene, J. Appl. Phys. **92**, 5084 (2002).

[29] G. M. Matenoglou, L. E. Koutsokeras, Ch. E. Lekka, G. Abadias, S. Camelio, G. A. Evangelakis, C. Kosmidis, and P. Patsalas, J. Appl. Phys. **104**, 124907 (2008).

[30] J.-L. Ruan, J.-L. Huang, H.-H. Lu, J. S. Chen, and D.-F. Lii, Thin Solid Films **519**, 4987 (2011).

[31] V. Hauk, W. K. Krug, R W M Oudelhoven, and P. Pintschovius, Z. Metallk **79**, 159 (1988).

[32] I. C. Noyan and J. B. Cohen, in *Residual Stress, Measurement by Diffraction and Interpretation* (Springer-Verlag, New York, 1987).

[33] G. Abadias, Surf. Coat. Technol. **202**, 2223 (2008).

[34] A. Fillon, G. Abadias, A. Michel, and C. Jaouen, Thin Solid Films **519**, 1655 (2010).

[35] F. Nizzoli, J. R. Sandercock, G. K. Horton, and A. A. Maradudin, *Dynamical Properties of Solids* (Elsevier, North Holland, 1990) pp. 281–335.

[36] P. Djemia, F. Ganot, P. Moch, V. Branger, and P. Goudeau, J. Appl. Phys. **90**, 756 (2001).

[37] A. Kueny and M. Grimsditch, Phys. Rev. B **26**, 4699 (1982).

[38] G. W. Farnell and E. Adler, *Physical Acoustics*, edited by W. P. Mason, and R. N. Thurston (Academic, New York, 1972), Vol. 9.

[39] B. A. Auld, *Acoustic Fields and Waves in Solids* (Wiley, New York, 1973), Vols. 1 and 2.

[40] P. Djemia, A. Fillon, G. Abadias, A. Michel, and C. Jaouen, Surf. Coat. Technol. **206**, 1824 (2011).

[41] S. H. Wei, L. G. Ferreira, J. E. Bernard, and A. Zunger Phys Rev B **42**, 9622 (1990).

[42] P. H. Mayrhofer, D. Music, and J. M. Schneider, J. Appl. Phys. **100**, 094906 (2006).

[43] F. Tian, J. D'Arcy-Gall, T. Y. Lee, M. Sardela, D. Gall, I. Petrov, and J. E. Greene, J. Vac. Sci. Technol. A **21**, 140 (2003).

[44] H. Kindlund, J. Lu, J. Jensen, I. Petrov, J. E. Greene, and L. Hultman, J. Vac. Sci. Technol. **31**, 040602 (2013).

[45] D. Holec, L. Zhou, R. Rachbauer, and P. H. Mayrhofer, J. Appl. Phys. **113**, 113510 (2013).

[46] F. Tasnádi, M. Oden, and I. A. Abrikosov, Phys Rev B **85**, 144112 (2012).

[47] J. P. Perdew, K. Burke, and M. Ernzerhof, Phys. Rev. Lett. **77**, 3865 (1996).

[48] G. Kresse and J. Furthmuller, Phys. Rev. B **54**, 11169 (1996).

[49] P. E. Blöchl, Phys. Rev. B **50**, 17953 (1994).

[50] H. J. Monkhorst and J. D. Pack, Phys. Rev. B **13**, 5188 (1976).

[51] See Supplemental Material at http://link.aps.org/supplemental/10.1103/PhysRevB.90.144107 for more details on computed elastic properties, additional XRD data and nanoindentation tests.

[52] P. Blaha, K. Schwarz, G. K. H. Madsen, D. Kvasnicka, and J. Luitz, WIEN2k: *An Augmented Plane Wave+Local Orbitals Program for Calculating Crystal Properties* (T.U. Wien, Austria, 2001).

[53] R. Hill, Proc. Phys. Soc. (London) A **65**, 349 (1952).

[54] D. Baral, J. E. Hilliard, J. B. Ketterson, and K. Miyano, J. Appl. Phys. **53**, 3552 (1982).

[55] F. Birch, Phys. Rev. **71**, 809 (1947).

[56] A. J. Perry, Thin Solid Films **193-194**, 463 (1990).

[57] L. E. Koutsokeras and G. Abadias, J. Appl. Phys. **111**, 093509 (2012).

[58] T. Mashimo, S. Tashiro, T. Toya, M. Nishida, H. Yamazaki, S. Yamaya, K. Oh-Ishi, and Y. Syono, J. Mater. Sci. **28**, 3439 (1993).

[59] S. K. R. Patil, N. S. Mangale, S. V. Khare, and S. Marsillac, Thin Solid Films **517**, 824 (2008).

[60] E. I. Isaev, S. I. Simak, I. A. Abrikosov, R. Ahuja, Yu. Kh. Vekilov, M. I. Katsnelson, A. I. Lichtenstein, and B. Johansson, J. Appl. Phys. **101**, 123519 (2007).

[61] E. Zhao and Z. Wu, J. Solid State Chem. **181**, 2814 (2008).

[62] M. B. Kanoun and M. Jaouen, J. Phys. Cond. Matter. **20**, 085211 (2008).

[63] Kh. Bouamama, P. Djemia, D. Faurie, and G. Abadias, J. Alloys Comp. **536**, S138 (2012).

[64] P. Djemia, M. Benhamida, Kh. Bouamama, L. Belliard, D. Faurie, and G. Abadias, Surf. Coat. Technol. **215**, 199 (2013).

[65] G. Fournet, J. Phys. **14**, 374 (1953).

[66] C.-S. Shin, Y.-W. Kim, D. Gall, J. E. Greene, and I. Petrov, Thin Solid Films **402**, 172 (2002).

[67] S. Noda, K. Tepsanongsuk, Y. Tsuji, Y. Kajikawa, Y. Ogawa, and H. Komiyama, J. Vac. Sci. Technol. A **22**, 332 (2004).

[68] I. A. Saladukhin, G. Abadias, A. Michel, S. V. Zlotsk, V. V. Uglov, G. N. Tolmachova, and S. N. Dub, Thin Solid Films **538**, 32 (2013).

[69] J. Musil, Surf. Coat. Technol. **207**, 50 (2012).

[70] G. Abadias, L. E. Koutsokeras, Ph. Guerin, and P. Patsalas, Thin Solid Films **518**, 1532 (2009).

[71] G. Abadias, L. E. Koutsokeras, A. Siozios, and P. Patsalas, Thin Solid Films **538**, 56 (2013).

[72] J. F. Ziegler, J. P. Biersack, and U. Littmark, *The Stopping and Range of Ions in Solids* (Pergamon, New York, 1985), http://www.srim.org.

[73] A. Anders, Thin Solid Films **518**, 4087 (2010).

[74] S. Mahieu and D. Depla, J. Phys. D: Appl. Phys. **42**, 053002 (2009).

[75] R. Daniel, K. J. Martinschitz, J. Keckes, and C. Mitterer, Acta Mater. **58**, 2621 (2010).

[76] G. Abadias and Ph. Guerin, Appl. Phys. Lett. **93**, 111908 (2008).

[77] G Abadias, W P Leroy, S Mahieu, and D Depla, J. Phys. D: Appl. Phys. **46**, 055301 (2013).

[78] Y. Le Page and P. Saxe, Phys. Rev. B **63**, 174103 (2001).

[79] X.-J. Chen, V. V. Struzhkin, Z. Wu, M. Somayazulu, J. Qian, S. Kung, A. N. Christensen, Y. Zhao, R. E. Cohen, H.-K. Mao, and R. J. Hemley, Proc. Natl. Acad. Sci. USA **102**, 3198 (2005).

[80] B. D. Fulcher, X. Y. Cui, B. Delley, and C. Stampfl, Phys Rev B **85**, 184106 (2012).

[81] S. Nagao, K. Nordlund, and R. Nowak, Phys. Rev. B **73**, 144113 (2006).
[82] M. G. Brik and C. G. Ma, Comput. Mater. Sci. **51**, 380 (2012).
[83] M. Born, K. Huang, *Dynamical Theory of Crystal Lattices* (Clarendon Press, Oxford, London, 1954).
[84] M. B. Kanoun, P. Hermet, and S. Goumri-Said, J. Phys. Chem. C **116**, 11746 (2012).
[85] M. H. Ledbetter, *Elastic Properties*, in Materials at Low Temperatures, edited by R. P. Reed and A. F. Clark (American Society for Metals, Metals Park, OH, 1983).
[86] S-H Jhi, S. S. G. Louie, and M. L. Cohen, J. Ihm, Phys. Rev. Lett. **86**, 3348 (2001).
[87] C-S Shin, D. Gall, N. Hellgren, J. Patscheider, I. Petrov, and J. E. Greene, J. Appl. Phys. **93**, 6025 (2003).